University of California
Santa Barbara

Filtration and Clogging Dynamics in Suspensions: Mechanisms, Models, and Optimization

A thesis submitted in partial satisfaction
of the requirements for the degree

Master's of Science
in
Mechanical Engineering

by

Justin Maddox

Committee in charge:

Professor Alban Sauret, Chair
Professor Eckart Meiburg
Professor Todd Squires
Professor Emilie Dressaire

December 2024

The Dissertation of Justin Maddox is approved.

Professor Eckart Meiburg

Professor Todd Squires

Professor Emilie Dressaire

Professor Alban Sauret, Committee Chair

December 2024

Filtration and Clogging Dynamics in Suspensions: Mechanisms, Models, and Optimization

by

Justin Maddox

Abstract

Filtration and Clogging Dynamics in Suspensions: Mechanisms, Models, and Optimization

by

Justin Maddox

The filtration behavior of suspensions in various physical systems presents both challenges and opportunities. In confined flows, filtration is often an unintended and undesired effect, such as in irrigation systems, where flowing suspended particles can become trapped internally, leading to a gradual clogging effect. Conversely, when it is necessary to remove certain particle types from a suspension, the filtration effect can be desirable and useful. This work aims to use experimental methods to further the understanding of suspension filtering/clogging and empower others with methods to either prevent or leverage the filtration of suspensions, depending on their needs.

The first part of this thesis examines the filtration and sorting of fiber-type suspensions based on fiber size; this presents a challenging problem because of the fibers' two characteristic dimensions, L and D. However, the process of dip coating by immersing a substrate in a suspension bath presents some interesting sorting capabilities; as the substrate is withdrawn, the meniscus acts as a filter which repels certain particles from the liquid bath and accepts others, becoming entrained in the coating film. With flat substrates, particles are categorically sorted by diameter; however, the curved meniscus created by withdrawing a cylindrical substrate forces a preferential fiber alignment which can sort a well-mixed fiber suspension by particle length. This length sorting process is investigated and recommendations are made on best practices.

The focus then turns to the clogging behavior of rigid fiber suspensions flowing around

a 90-degree bend. The fiber suspensions travel at constant flow rate through a channel with a uniform cross-section, and their movement is analyzed as they pass through the bend, where both the channel width and radii of curvature are precisely controlled. Fibers are characterized as "clog", "slip", or "no-slip" cases, and numerical methods are used to produce predictive models of clogging. Additionally, guidelines are presented for designing clog-resistant bends within millifluidic systems dispensing fiber suspensions.

Finally, a comprehensive review of clogging in drip irrigation systems is presented from a fluid mechanics point-of-view, studying specifically the phenomena of physical clogging by sand, silt, and clay type particles. The current research in the area of improving anti-clogging performance of drip emitters is investigated, highlighting the role of both active and passive methods in decreasing the replacement rate of drip emitters due to clogs. This review gives a direction to possible future studies on geometry optimization of drip emitters, and presents the current best practices in extending the lifetime of drip irrigation systems using fluid mechanics principles.

Contents

Abstract iv

1 Introduction 1
- 1.1 Suspension Flow, Filtration, and Clogging . . . 1
- 1.2 Permissions and Attributions . . . 3

2 Capillary Sorting of Fiber Suspensions by Dip Coating 4
- 2.1 Introduction . . . 4
- 2.2 Methods . . . 7
- 2.3 Flat substrate: Sorting by Diameter . . . 10
- 2.4 Cylindrical Substrate: Sorting by Length. . . . 11
- 2.5 Discussion . . . 15
- 2.6 Conclusions . . . 18

3 Transport and Clogging of Fibers in Millifluidic Channels 21
- 3.1 Introduction . . . 21
- 3.2 Methodology . . . 25
  - 3.2.1 Experimental Methods . . . 25
  - 3.2.2 Numerical Methods . . . 28
- 3.3 Results . . . 32
  - 3.3.1 Phenomenology: Clogging or Not Clogging? . . . 32
  - 3.3.2 Clogging Probability in the Bent Channel . . . 37
  - 3.3.3 Influence of Channel Geometry . . . 39
  - 3.3.4 Estimating the Threshold Fiber Lengths for Clogging . . . 42
- 3.4 Conclusion . . . 44

4 Fluid Mechanics and Clogging in Drip Emitters 47
- 4.1 Introduction . . . 47
- 4.2 Geometry of Drip Emitters . . . 51
- 4.3 Physical Clogging Mechanisms . . . 54
  - 4.3.1 Experimental Tests . . . 54

4.3.2 Physical Clogging of Large Particles (Sand, Silt) 56
4.3.3 Physical Clogging of Small Particles (Clays) 57
4.4 Strategies to Mitigate Clogging 60
4.4.1 Active Strategies to Prevent Physical Clogging 61
4.4.2 Passive Strategies to Prevent Physical Clogging 63
4.5 Conclusion and Future Directions 65

5 Conclusion **67**

Bibliography **70**

Chapter 1

Introduction

1.1 Suspension Flow, Filtration, and Clogging

The filtration and transport of particulate suspensions are fundamental processes in both natural and industrial systems. These phenomena exhibit duality, offering significant opportunities when filtration is desirable while posing challenges when clogging disrupts intended flows. This thesis investigates these dynamics, focusing first on anisotropic fiber-type suspensions and later on natural wastewater suspensions containing sands, silts, and clays, along with their interactions with flow geometries and filtration systems.

In many industries, filtration is a key method to purify liquids, separate particles, and control size distributions [1, 2, 3, 4]. Conventional methods, such as sieving, centrifugal filtration, and cross-flow filtration, are often effective for spherical particles [5, 6]. However, the filtration of anisotropic particles, such as fibers, presents unique challenges due to their multiple characteristic dimensions. Chapter 2 examines capillary filtration via dip coating, demonstrating a promising approach for sorting fibers based on either diameter or length [7]. By leveraging the interplay between capillary forces, coating film thickness and shape, and particle geometry, this technique offers a novel solution for sort-

ing fiber-based suspensions by length. This section explores the conditions under which such methods achieve efficient filtration, optimizing factors such as substrate geometry and withdrawal velocity to enhance sorting capabilities.

Conversely, the unintended accumulation of particles can lead to clogging in confined flows, disrupting processes across various applications, such as additive manufacturing and biomedical systems [4, 8, 9]. While extensive studies have addressed clogging by spherical particles, anisotropic particles such as fibers introduce additional complexities [10, 11, 12, 13]. Chapter 3 investigated the clogging arising from fiber suspensions flowing around a millifluidic scale 90-degree bend. Notably, the fiber length and initial position in the channel significantly affect clogging probabilities, particularly in systems with bends or irregular geometries. This work examines the critical parameters influencing fiber transport and clogging, aiming to provide predictive models and design guidelines for more resilient fluidic systems.

Finally, in chapter 4, the attention shifts to drip irrigation, specifically the clogging of drip emitters [14, 15, 16]. By examining real wastewater-type suspensions under controlled conditions, strategies are identified to mitigate particle accumulation based on specific application needs. These insights contribute to a deeper understanding of suspension dynamics, advancing the design of systems capable of resisting filtration effects. By investigating drip irrigation from a fluid mechanics perspective, this work offers a framework for addressing the challenges that currently hold back a critical water-saving technology.

1.2 Permissions and Attributions

1. The content of chapter 2 is the result of a collaboration with Alban Sauret, and has previously appeared in *Physical Review Fluids*.
   https://doi.org/10.1103/PhysRevApplied.22.034071

2. The content of chapter 3 is the result of a collaboration with Thomas Nguyen, Harishankar Manikantan, and Alban Sauret. [Pre-publication draft]

3. The content of chapter 4 is the result of a collaboration with Camron Hosseini and Alban Sauret. [Pre-publication draft]

Chapter 2

Capillary Sorting of Fiber Suspensions by Dip Coating

2.1 Introduction

Filtration of particulate suspensions is critical in many industries as a method of purifying liquids, controlling particle sizes, and separating groups of particles [1, 2, 3, 4]. Some of the most commonly used methods are sieving, where the fluid passes through a filter of certain pore size [10]; centrifugal filtration, where centrifugal force is used to filter particles based on density [5]; and cross-flow filtration, where flow is tangential to a membrane and a transmembrane pressure differential is responsible for pulling smaller particles out of the flow [6]. These standard filtration methods can struggle with anisotropic particles as they present two lengthscales that can be defined, for instance, through a minimum and a maximum Feret diameter [17, 18, 19].

A potential solution to filter anisotropic particles, specifically fibers, is capillary filtration using a dip coating process. The principle is that a substrate is submersed within a suspension bath, and based on the withdrawal velocity of the substrate and the proper-

ties of the interstitial fluid, only particles below a certain threshold size will be entrained in the liquid film coating the substrate after removal [20, 21, 22, 23]. Previous works have demonstrated the efficacy of sorting spherical particles using dip coating with a planar substrate [24, 25] and cylindrical substrates [26, 27]. These sorting methods rely on the importance of the size of the particle compared to the size of the capillary film. Such interplay between liquid/air interfaces and solid particles have also been considered for liquid thread [28, 29, 30, 31, 32] and films [33, 34].

To provide some physical context, after a substrate has been immersed into a liquid bath, upon withdrawal, it becomes coated with a thin liquid film whose thickness, h, depends on the withdrawal velocity U, the properties of the liquid (surface tension γ, density ρ, dynamic viscosity μ), and the surface properties (geometry, roughness, etc. [35, 36]). For a planar substrate and a Newtonian fluid, the Landau-Levich-Dejarguin law predicts:

$$h = 0.94\,\ell_c\,\mathrm{Ca}^{2/3}, \tag{2.1}$$

where $\ell_c = \sqrt{(\gamma/(\rho g)}$ is the capillary length and $\mathrm{Ca} = \mu U/\gamma$ the capillary number [37, 38]. For cylindrical substrates, the coating thickness involves the Goucher number, $\mathrm{Go} = R_s/\ell_c$ [39, 40, 41, 36] (where R_s is the radius of the substrate) and can be estimated through [26]:

$$\frac{h}{R_s} = \frac{1.34\,\mathrm{Ca}^{2/3}}{1 + 2.53\,\mathrm{Go}^{1.85}/[1 + 1.79\,\mathrm{Go}^{0.85}]} \tag{2.2}$$

The filtering of spherical non-Brownian particles has been shown to depend on h^* [42, 24], which corresponds to the thickness of the liquid at the point where the static meniscus ends and the dynamic meniscus begins, also known as the stagnation point [43]. This point also corresponds to the location that separates the flow into two regions: a region that continues into the coating film and a region where the fluid recirculates into the liquid bath. The particles that make it past the stagnation point and that are

of size comparable to h^* see a sharp increase in frictional forces, which allows for the overcoming of capillary forces [44]. In the limit of small capillary numbers, the thickness at the stagnation point and the film thickness are related through $h^* \approx 3h$ [26]. For spherical particles, the sorting by diameter sorting occurs when $h^* \lesssim d/2$ [24]. From a qualitative point of view, the mechanism associated with the capillary sorting of particles is similar to a dynamic "filter" whose size is governed by the film thickness h (and thus by the thickness at the stagnation point h^*). As the substrate is withdrawn from the suspension bath, the liquid film creates a "channel" that particles must enter to become entrained, bounded on one side by the substrate and on the other side by the air-liquid interface [25].

In the case of fiber suspensions, the situation becomes more complex as, in addition to the diameter d, a new lengthscale is introduced: the length L. A recent study suggested that for dip coating with cylindrical substrates, fibers of length larger than the diameter of the substrate were entrained only at larger withdrawal velocities than predicted based on their diameter [7]. This observation suggests that using different kinds of substrates (flat or cylindrical) could potentially control whether sorting fiber suspensions by capillary filtration occurs through the diameter d or the length of the fibers L and could thus provide a unique sorting platform. In this chapter, we examine if such a filtration method is possible, and we report the conditions under which this could be realized. We first present our experimental methods before considering the filtration by diameter with a flat substrate. In a second time, using a cylindrical substrate, we report the condition and the efficiency of length-based filtration. Finally, we discussed the limits of this method and how to optimize the filtration process.

2.2 Methods

Schematics of the experimental setup are shown in Figs. 2.1(a)-(b). The suspensions are made of non-Brownian nylon fibers of diameter $200\,\mu\text{m} \leq d \leq 400\,\mu\text{m}$ and length $1.5\,\text{mm} \leq L \leq 4.5\,\text{mm}$ dispersed in Fluorosilicone (FMS-221, Gelest), a Newtonian fluid of viscosity $\mu_\text{f} = 109\,\text{mPa.s}$, surface tension $\gamma = 21\,\text{mN.m}^{-1}$ and density $\rho_\text{f} = 1160\,\text{kg.m}^{-3}$. The fibers used are cut to the desired length by mechanical chopping (WC302 Automatic Wire Cutter, The Eraser Company), resulting in a well-controlled average length L and a standard deviation on the length of 0.25 mm. Due to the mechanical chopping, the edges of the fibers are not perfectly cylindrical, but, for instance, a little bit flattened irregularly. Nevertheless, we did not observe any effects of the edge geometry on the sorting process. In our experiments, no deformation of the fibers was observed for any aspect ratio considered. The density of the liquid is close enough to the density of the fibers ($\rho \simeq 1150\,\text{kg.m}^{-3}$) so that buoyancy effects can be neglected over the timescale of the experiments. The volume fraction of fibers used, $\phi = V_\text{fib}/V_\text{tot} = 0.5\%$, ensures that we remain in the dilute regime [45]. The suspensions are initially mixed overnight using magnetic stirrer bars and mixed for 5 minutes between trials. Using optical absorbance, we ensured that our experimental protocol led to fibers initially homogeneously dispersed in the suspension bath.

We perform the experiments with two substrate geometries: a planar substrate that consists of a glass plate (7mm thick, 50mm wide, 70 mm length; see figure 2.1(c)) and a cylindrical substrate setup consisting of an array of three rods (each of radius $R_\text{s} = 1.2\,\text{mm}$; see figure 2.1(d)), withdrawn simultaneously from the suspension bath. The substrates are withdrawn from the suspension bath using a linear translation stage (Thorlabs NRT150 linear stepper motor) at a velocity ranging from $2.5\,\text{mm.s}^{-1}$ to $20\,\text{mm.s}^{-1}$ over a distance of 30 mm. In both cases, between trials, the substrates were cleaned using

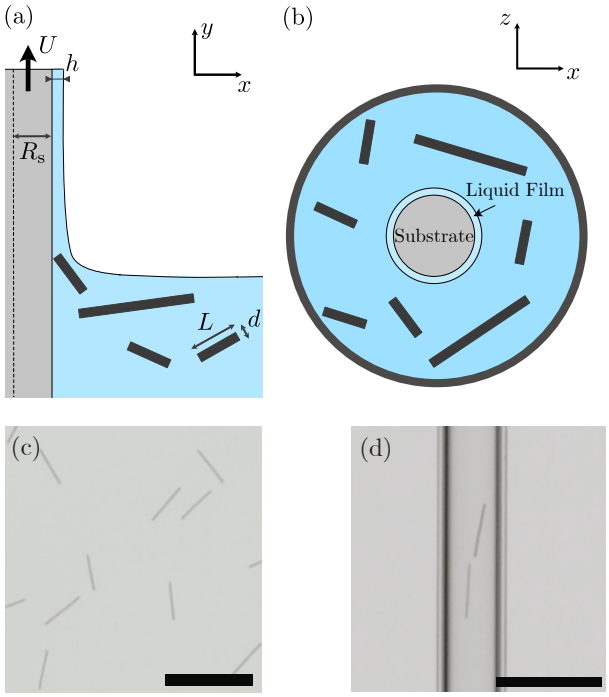

Figure 2.1: (a) Side and (b) top view schematics of the dip coating process with a suspension of fibers of diameter d and two different lengths L_1 and L_2. Note that the size of the fibers, the substrate, and the meniscus are not to scale. (c)-(d) Examples of entrainment of fibers on (c) a flat substrate where no preferential orientation is observed and (d) on a rod where the fibers entrained are of length comparable to the substrate diameter and thus mainly align with the axis of the rod.

isopropyl alcohol, rinsed with Deionized (DI) water, and dried using compressed air.

After each trial, the number of particles entrained was measured visually by examining the substrate over the entire length that had been withdrawn from the liquid. We should emphasize that over the time scale of the experiment and the measurement of the fiber entrained, we did not observe any significant sliding down of the fibers along the substrate. We performed experiments with a single population of fibers to determine the threshold capillary number corresponding to each fiber geometry and to study how the number of particles entrained depends on the withdrawal velocity. For the experiments with mixed suspensions, the liquid bath contains two different fiber geometries, each at an equal volume fraction. The results of these tests were used to determine the efficiency of

sorting two different fiber lengths or diameters. In the following, each data point reported in the different figures consists of 60 dip coating trials, *i.e.*, withdrawal of the substrate, and counting the number of fibers entrained.

We introduce different parameters to describe our results. The threshold Capillary number, $\mathrm{Ca}^* = \mu_\mathrm{f} U^*/\gamma$ refers to the threshold value at which a given geometry of fiber begins to be entrained for a specific substrate (U^* is the threshold capillary number). We consider here the capillary number based on the viscosity of the interstitial fluid μ_f since the volume fractions ϕ used in this study are very small, so the change in viscosity can be neglected [45, 46]. The effects of the substrate size compared to the fiber lengths are captured through a normalized fiber length, $L^* = L/2R_\mathrm{s}$, corresponding to the ratio of fiber length to the substrate diameter (for a flat plate, $L^* = 0$). We also define the normalized sorting efficiency as the difference between the mass of 'small' fibers entrained, m_S, and the mass of 'large' fibers entrained, m_L (where 'small' and 'large' can refer to the diameter or to the length depending on the situation) rescaled by the total mass of all fibers entrained:

$$\eta = \frac{m_\mathrm{S} - m_\mathrm{L}}{m_\mathrm{S} + m_\mathrm{L}} \tag{2.3}$$

Therefore, $\eta = 1$ refers to perfect sorting, and $\eta = 0$ to no sorting at all. Note that here, the volume fraction of both fiber populations is the same. Finally, we define $\phi_\mathrm{F}/\phi_\mathrm{U}$ defined as the average volume fraction of particles entrained in the liquid film on the substrate post-withdrawal rescaled by the unfiltered volume fraction of particles in the suspension bath.

2.3 Flat substrate: Sorting by Diameter

We first consider a suspension made of fibers of similar length ($L = 1.5\,\text{mm}$) but two different diameters $d = 200\,\mu\text{m}$ and $d = 400\,\mu\text{m}$. The fibers are mixed at a 1:1 ratio, occupying a volume fraction $\phi = 0.5\%$. Because all fibers were cut from a continuous wire of approximately constant diameter, there was no notable distribution of sizes within each diameter group. Dip coating was performed with a planar substrate at various velocities, and we measured the distribution of fibers found on the substrate post-withdrawal.

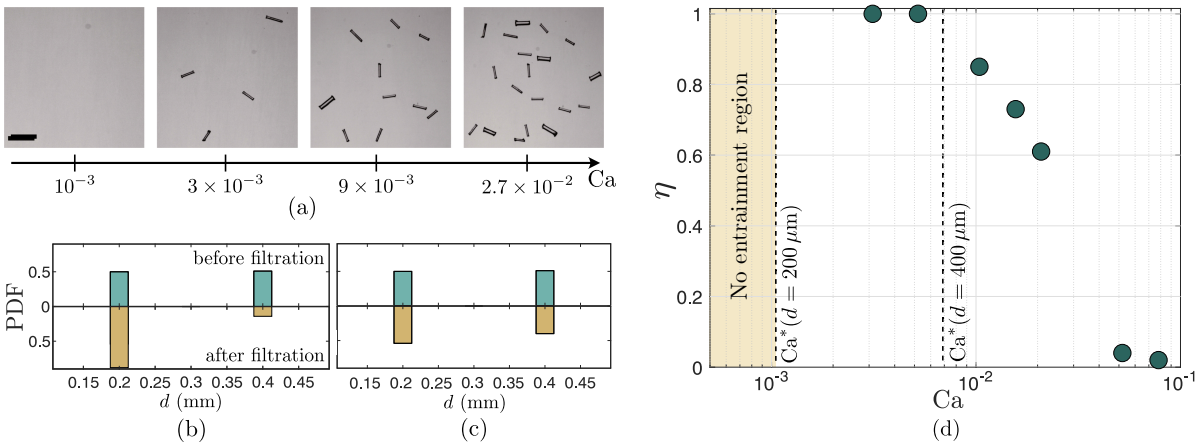

Figure 2.2: (a) Examples of post-filtration fiber distributions observed on a flat substrate for increasing capillary numbers and an initial suspension made of fibers of length $L = 1.5\,\text{mm}$ and diameter $d = 200\,\mu\text{m}$ and $d = 400\,\mu\text{m}$. From left to right: No entrainment, perfect sorting, high-efficiency sorting, low-efficiency sorting. Scale bar is 3 mm. (b)-(c) Examples of probability density functions of the fiber diameter before (top PDF) and after (bottom PDF) for (b) a good-efficiency sorting at $\text{Ca} = 10^{-2}$ and (c) low-efficiency sorting at $\text{Ca} = 5 \times 10^{-2}$ for the same suspension than in (a). (d) Evolution of the diameter sorting efficiency η as a function of the capillary number with a planar substrate and the same suspension. The shaded area denotes the region with no fiber entrainment. The vertical dashed lines indicate the threshold capillary numbers of each fiber type contained within the suspension. The suspension consists of $L = 1.5\,\text{mm}$ long fibers, with a 0.5% volume fraction of $d = 200\,\mu\text{m}$ diameter fibers and a 0.5% volume fraction of $d = 400\,\mu\text{m}$ diameter fibers.

Fig. 2.2(a) shows examples of the results of the filtration process when varying the withdrawal velocity and, thus, the capillary number. At very low values of Ca ($\text{Ca} = 10^{-3}$ in the example presented here), no fiber entrainment occurs because each of the two

fibers has its own threshold capillary number, Ca^*, larger than $Ca = 10^{-3}$, all particles are filtered out. At values of Ca between the individual Ca^* values of each fiber, there is theoretically perfect sorting, as seen here for $Ca = 3 \times 10^{-3}$. At values of Ca above Ca^* of both particles ($Ca = 9 \times 10^{-3}$ in the present example), there are some sorting effects, but its efficiency decreases as Ca increases further. We report in Figs. 2.2(b) and 2.2(c) a more quantitative analysis: the probability density functions of the fiber diameter before (*i.e.*, in the suspension) and after the withdrawal for $Ca = 10^{-2}$ and $Ca = 5 \times 10^{-2}$, respectively. As suggested by the observations in Fig. 2.2(a), we observe that the filtration efficiency decreases as the capillary number is increased as fewer fibers with a diameter $d = 400\,\mu$m are filtered out [Fig. 2.2(c)].

Fig. 2.2(d) shows that using a planar substrate, it is possible to achieve high efficiencies of diameter sorting between fibers of nearly equal length. Notably, 100% diameter sorting efficiency was achieved for the trials between $Ca \sim 10^{-3}$ and $Ca \sim 7 \times 10^{-3}$, which corresponds to capillary numbers between the two thresholds of entrainment for 1.5 mm fibers: $Ca^*(d = 200\,\mu\text{m}) < Ca < Ca^*(d = 400\,\mu\text{m})$. At capillary numbers above the threshold value for both fibers, there is a drop in sorting efficiency η, eventually approaching 0%, *i.e.*, value associated with complete randomness and no sorting capability, around $Ca \simeq 10^{-1}$ for the fibers considered here. In the present case, this value of Ca corresponds to a film thickness of order 300μm and a thickness at the stagnation point of around 900μm, so that the meniscus does not act as a filter anymore, allowing all the fibers to flow through.

2.4 Cylindrical Substrate: Sorting by Length.

To explore the possibility of sorting fibers having the same diameters but different lengths, we first performed entrainment experiments using cylindrical substrates of radius

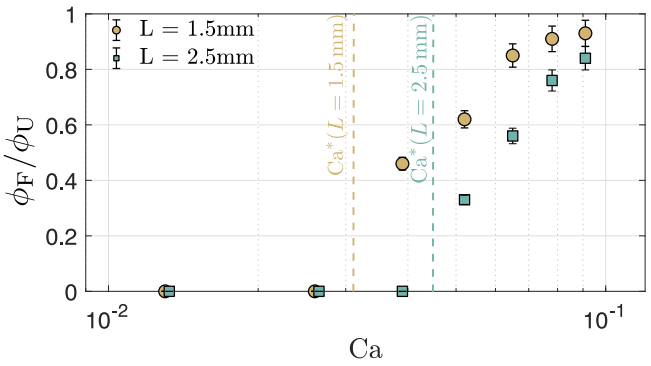

Figure 2.3: Evolution of the volume fraction of fibers entrained in the liquid film ϕ_F rescaled by the volume fraction of fibers in the suspension bath, $\phi_U = 0.5\%$, as a function of the capillary numbers for fibers of diameter $d = 200\,\mu$m, and length $L = 1.5\,$mm (blue circles) and $L = 2.5\,$mm (orange squares). The vertical dashed lines indicate the threshold capillary numbers of each fiber type for experiments with only one fiber population in suspension.

$R_s = 1.2\,$mm and two different fiber lengths, $L = 1.5\,$mm and $L = 2.5\,$mm separately. The results reported in Fig. 2.3 show that, despite having the same diameters, the threshold Capillary numbers are different: $\mathrm{Ca}^*(\mathrm{L} = 1.5\,\mathrm{mm}) \simeq 3 \times 10^{-2}$ and $\mathrm{Ca}^*(\mathrm{L} = 2.5\,\mathrm{mm}) \simeq 5 \times 10^{-2}$. This is due to the fact that $L^* = L/(2\,R_s)$ is different for each population of fibers and the fibers have to reorient to enter the liquid film [7]. Therefore, theoretically, the ideal range of parameters for sorting these two populations of fibers by length with a cylindrical substrate of radius $R_s = 1.2\,$mm would be for $3 \times 10^{-2} < \mathrm{Ca} < 5 \times 10^{-2}$. Fig. 2.3 also shows that ϕ_F/ϕ_U, *i.e.*, the ratio of the volume fraction of fibers filtered rescaled by the volume fraction in the initial suspension increases with Ca. When $\phi_F/\phi_U \to 0$, no fibers are entrained on the substrate and when $\phi_F/\phi_U \to 1$, the meniscus does not filter any fiber, which are then all entrained in the film. Here, we observe that for values of Ca approaching 10^{-1}, both fiber populations are poorly filtered, each reaching volume fraction ratios of nearly 1, meaning that no separation by length would occur.

Following these tests with each fiber geometry, we then considered the possibility to filter a suspension presenting two populations of fibers of $d = 200\,\mu$m and average

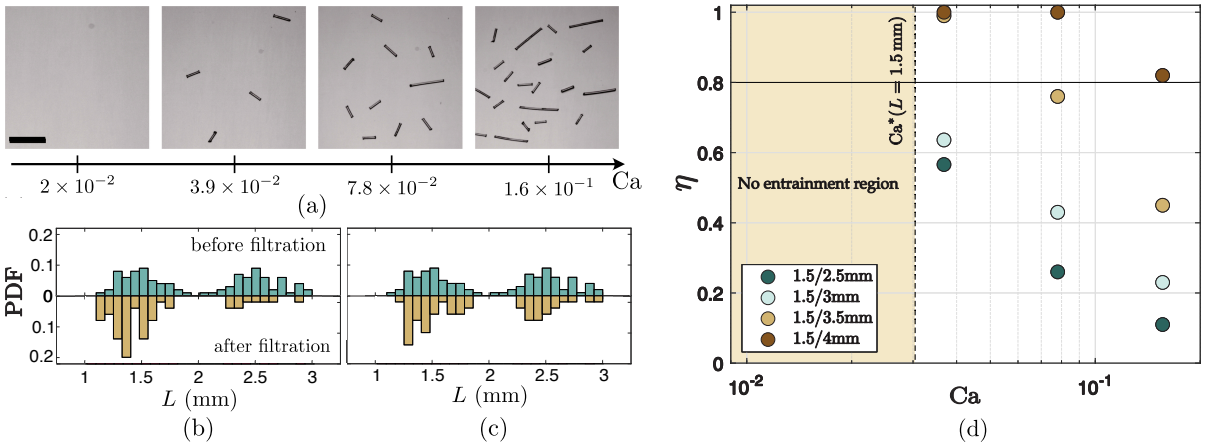

Figure 2.4: (a) Examples of post-filtration fiber distributions observed on a cylindrical substrate for various capillary numbers. From left to right: No entrainment, perfect sorting, high-efficiency sorting, low-efficiency sorting. Scale bar is 3 mm. (b)-(c) Examples of probability density functions of the fiber length before (top PDF) and after (bottom PDF) for (b) a good-efficiency sorting at $\mathrm{Ca} = 3.9 \times 10^{-2}$ and (c) low-efficiency sorting at $\mathrm{Ca} = 7.8 \times 10^{-2}$. In (a)-(c), the initial suspension is made of fibers of $d = 200\,\mu$m and average lengths $L = 1.5$ mm and $L = 2.5$ mm. (d) Comparison of length sorting efficiency between various fiber lengths demonstrating a downward trend with increasing capillary numbers. The red area denotes the region of no fiber entrainment. All trials were performed with fibers of 200 μm diameter and a substrate radius of $R_\mathrm{s} = 1.2$ mm. For all data points, the suspension consisted of 0.5% of 1.5 mm long fibers and 0.5% of the other length by volume fraction.

lengths $L = 1.5$ mm and $L = 2.5$ mm, respectively. Qualitatively, Fig. 2.4(a) shows that filtration is also observed here: (i) no fibers beyond the threshold capillary number of both fiber populations, (ii) a regime where almost only short fibers are entrained, (iii) increasing the capillary number leads to the entrainment of more long fibers as well, until (iv) entraining almost the same composition than the liquid bath at large capillary number (corresponding to $\phi_\mathrm{F}/\phi_\mathrm{U} \to 1$ in Fig. 2.3).

More quantitatively, two examples of the distribution of fiber lengths are shown in Figs. 2.4(b) and 2.4(c) for $\mathrm{Ca} = 3.9 \times 10^{-2}$ and $\mathrm{Ca} = 7.8 \times 10^{-2}$, respectively. Before filtration, we observe a bimodal distribution of fiber lengths in both cases (top histograms) peaked around $L = 1.5$ mm and $L = 2.5$ mm. The deviation from the mean value comes from the initial cutting of the fibers to obtain the desired lengths. After the withdrawal

of the cylindrical substrate, we observe that the distribution skews more towards the 1.5 mm fibers for Ca $= 3.9 \times 10^{-2}$. We should emphasize that in this case, even with a high sorting efficiency, there are a few long fibers ($L = 2.5$ mm) that were entrained on the substrate at a capillary number below its threshold value. This observation is likely due to the collective entrainment of particles, as we shall discuss later. At larger capillary numbers, the filtered distribution is almost similar to the initial distribution in the liquid bath [Figs. 2.4(c)].

To explore a broader range of potential length sorting, the 1.5 mm fibers ($L^* = 0.63$) were also mixed with 3 mm, 3.5 mm, and 4 mm fibers, leading to $L^* = 1.25$, 1.46, and 1.67, respectively. For all the situations, capillary numbers of 3.9×10^{-2}, 7.8×10^{-2}, and 1.5×10^{-1} were tested. The purpose of these trials is to explore the evolution of the sorting efficiency η for different values of L^* and different ratios of fiber length (but the same diameter). Fig. 2.4(d) showed that, as expected, the trials at Ca $= 3.9 \times 10^{-2}$ has a higher efficiency than for larger capillary number, *e.g.*, Ca $= 7.8 \times 10^{-2}$. Fig. 2.4(d) also illustrates that when mixed with $L = 4$ mm fibers, the 1.5 mm fibers are perfectly sorted at both Ca $= 3.9 \times 10^{-2}$ and Ca $= 7.8 \times 10^{-2}$, indicating that this latter value is still lower than the entrainment threshold of the 4 mm fibers. At Ca $= 1.5 \times 10^{-1}$, none of the mixed suspensions are able to achieve perfect filtration, and the mix of 1.5 mm and 2.5 mm fibers showed a poor filtration. Considering the different mixes of fibers and a given capillary number, we observe that a suspension of greater length disparity has a higher sorting efficiency than those with two fibers of more similar length.

Since the threshold capillary number for a given cylindrical substrate increases with the fiber length, in particular when L^* becomes larger than unity, the value of L^* controls the filtering of a given population of fibers. Low values indicate a decrease in the influence of meniscus curvature around the cylindrical substrate on fiber behavior. The higher the value of L^*, the tighter the tolerance is for fiber orientation in order to fit within the

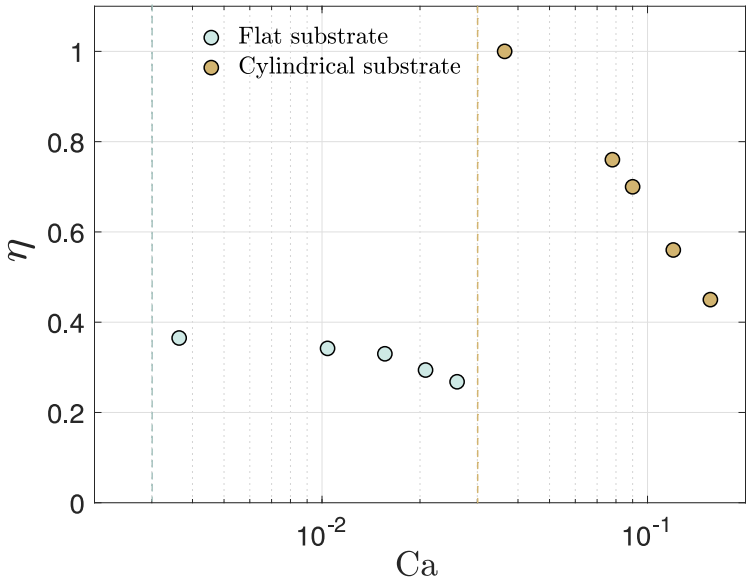

Figure 2.5: Evolution of the length sorting efficiency η for a planar (light green circles) and a cylindrical substrate (brown circles). The suspension consists of 0.25% of 1.5 mm long fibers and 0.25% of 3.5 mm long fibers and of diameters $d = 200\,\mu$m. The vertical dashed line indicates the capillary threshold for the entrainment of the short fibers for both geometries.

meniscus and become entrained. Our results suggest that a value of $L^* \geq 1$ is reasonable to achieve a good sorting efficiencies. Maximizing L^* as much as possible improves the filtering efficiency, but the main drawback to higher L^* values is that the threshold withdrawal velocities increase.

2.5 Discussion

The fibers used here are of length $L \gg h$, so that they will need some amount of reorientation to fit within the meniscus as viscous forces pull them upward or else be subjected to surface forces, which will push them back downward, as described in Ref. [7]. In addition, a key difference between planar and cylindrical substrates is the curvature in the horizontal direction (around the cylindrical substrates). Past experiments have shown

that planar substrates allow for most fibers to have their axis become along the meniscus near the entrainment threshold [7], thus allowing the coupling between capillary effects and the frictional force. Conversely, a cylindrical substrate has a curved film, which means that long fibers ($L^* \gtrsim 1$) must reorient such that their main axis becomes parallel to the axis of the substrate to become entrained. This means that for a cylindrical substrate, longer fibers must take a path of higher resistance to entrainment, fully rotating to the preferred orientation, and without an alternative lower resistance path like the planar substrate, longer fibers will be consistently repelled. As a result, the threshold capillary numbers for longer fibers ($L^* \gtrsim 1$) increases with L^*. The consequence of this difference is that attempting to sort by length with planar substrates is less efficient, as illustrated in Fig. 2.5. However, with cylindrical substrates, a better sorting efficiency can be achieved, as reported in Fig. 2.5 where when attempting to sort fibers of 200 μm diameter and length between 1.5 mm and 3.5 mm, a planar substrate (where $L^* = 0$) resulted in a peak efficiency of 36%, while a $R_s = 1.2$ mm radius cylindrical substrate (where $L^* = 0.6$ for the 1.5 mm fibers and $L^* = 1.4$ for the 3.5 mm fibers) resulted in a peak efficiency of 100%. We should emphasize that the difference in operating capillary numbers between the two substrates is due to the different evolution of the film thickness with Ca, as shown in Eqs. (2.1) and (2.2) for the flat and cylindrical substrates, respectively.

The results presented so far have shown that diameter and length sorting can be performed independently with a very good efficiency, given that the other parameter is held constant. We also performed experiments with fiber populations with both different lengths and diameters: $d = 330\,\mu$mm and $L = 1.5$ mm mixed with $d = 200\,\mu$m and $L = 3.5$ mm. Here, we also consider a case with $d = 200\,\mu$mm and $L = 1.5$ mm mixed with $d = 200\,\mu$m and $L = 3.5$ mm for comparison. The evolution of the efficiency η for both mixed populations is reported in Fig. 2.6.

At small values of Ca (Ca $\lesssim 0.1$ in the example here), a large difference between

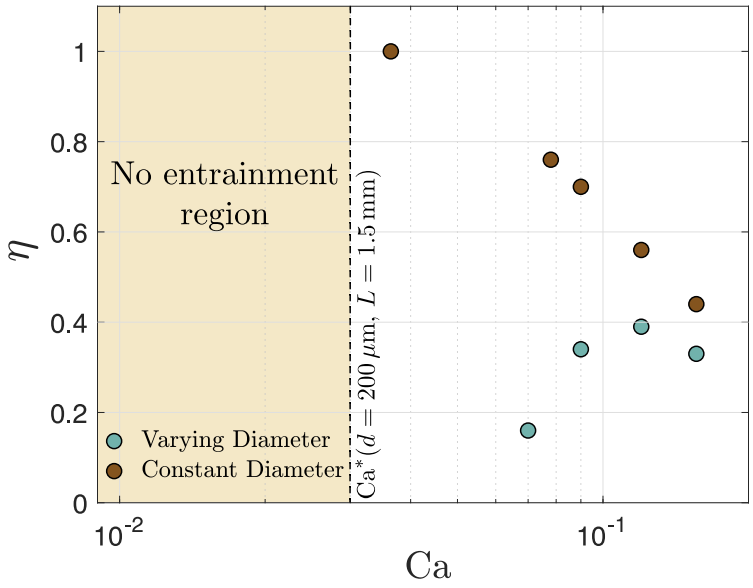

Figure 2.6: Comparison of the sorting efficiency for various values of Ca. The varying diameter dataset refers to dip coating experiments with a suspension with volume fractions of 0.25% of 0.33 mm diameter, 1.5 mm long fibers, and 0.25% of 200 μm diameter, 3.5 mm long fibers. Constant diameter dataset refers to dip coating experiments with a suspension with volume fractions of 0.25% 200 μm diameter, 1.5 mm long fibers, and 0.25% 200 μm diameter, 3.5 mm long fibers and serve as the control dataset to observe the relative difference in efficiency when the diameter is varied.

the efficiencies is observed in Fig. 2.6. While the experiments with a constant diameter exhibit a high efficiency, the experiments with two different fiber diameters initially show a very low efficiency, indicating that the diameter sorting effect is roughly of the same order as the length sorting effect. However, for higher values of Ca (Ca $\gtrsim 0.1$ here), as the ratio of film width to fiber diameter became larger, the diameter sorting effects became negligible for the two diameters considered here, and the two trials reached similar values, showing that the length sorting effect is at play.

A practical guideline when attempting to sort a suspension by length when different fiber diameters are present would be to first consider sorting using a planar substrate since the diameter sorting effects will usually be of higher order than length sorting effects. In a second time, for the different diameter populations, the sorting could be done with

cylindrical substrates as described earlier in this article. If the two-step filtration is not possible, it is desirable to operate at a Capillary number significantly greater than Ca^* for the largest diameter in the suspension so that the main filtration effect is by length.

2.6 Conclusions

Using a flat or a cylindrical substrate in a dip coating process, we have shown that it is possible to sort fiber suspensions by length or by diameter. Diameter sorting effects are prevalent when using a planar substrate, typically greatly outweighing length sorting effects. Mechanically, there is no difference in the process of sorting fibers by diameter using a planar substrate or using a cylindrical substrate if $L^* \ll 1$. The diameter sorting process provides a level of reliability that is typically greater than that of length sorting because fibers larger than the threshold size physically cannot pass through the filter; that is to say, it is not susceptible to statistical anomalies. The sorting by diameter is similar to the sorting considered in the past for spherical non-Brownian particles [25, 27]. Using the different dimensionless quantities introduced in the manuscript (capillary number, Goucher number, d/L and h/d allows to easily adapt the results to different interstitial fluids or fiber sizes.

The theoretical range of optimal efficiency is in the range of capillary numbers between the threshold values of each individual particle suspension. However, it is not always possible to achieve perfect sorting for a mixed suspension, especially if the ratio of the two nominal lengths is close to 1. Fig. 2.4 illustrates this point: at $Ca = 3.9 \times 10^{-2}$, the sorting efficiency of the mixed 1.5 mm and 2.5 mm suspension should have theoretically been 100%, but in practice, it is lower. This observation is similar to observations done in regular filters, where some suspensions cannot be sorted perfectly on the first trial because the geometries are too similar. When this is the case, one potential workaround

is to sort the same suspension several times, as theoretically, with enough iterations, an effective efficiency of nearly 100% can be achieved.

Even when a fiber suspension has a large enough disparity in length to ideally sort perfectly, volume fraction effects can lead to a decrease in efficiency due to the entrainment of clusters of particles [24]. Indeed, when the local volume fraction at the meniscus is too high, collective effects may appear, and the desired length fibers will form clusters that can become tangled with the undesired length and pass through the meniscus as one large aggregate [47]. Reducing the average volume fraction of the entire suspension will help to minimize this effect. Ideally, the volume fraction would be as low as possible; however, very low volume fractions lead to a much smaller average number of particles entrained per trial, which may be undesirable in creating a rapid filtering process. As such, the volume fraction chosen should provide an acceptable balance between filtering efficiency and process duration to meet their individual requirements.

To provide an efficient sorting by length using a cylindrical substrate, the best combination is to have one fiber population satisfying $L^* \leq 1$ and the other one $L^* \geq 1$. This threshold can be tuned by changing the radius R_s of the cylindrical substrate. The condition $L^* \geq 1$ enforces a preferential alignment that will delay the entrainment of the fiber. Our results also show that, when sorting by length, it is more efficient if the fiber diameter standard deviation is minimized. Given that diameter sorting effects can be of equal or higher order to length sorting, having a wide distribution of diameters allows some undesired fibers to be entrained.

In this section, we have outlined a systematic approach that can be used to achieve high-efficiency capillary diameter and length filtering. We should emphasize that various fundamental questions remain open that would allow to increase further the efficiency of the capillary sorting method presented here. For instance, the presence of surfactants is known to modify the streamlines in the liquid bath [43], which could tentatively lead to

new sorting effects. Additionally, most capillary sorting and filtering studies have been done with Newtonian fluids, and the extension to non-Newtonian rheology would be interesting to consider. Nevertheless, in summary, the method presented here provides a promising novel soft filtration strategy, which, if designed correctly, has the potential to achieve an efficient selective length or diameter sorting of elongated particles, illustrated here with fibers.

Chapter 3

Transport and Clogging of Fibers in Millifluidic Channels

3.1 Introduction

The transport of solid particles in tubing, channels, and nozzles is common in additive manufacturing [48, 49] biomedical systems [19], and food processing [50]. The particles involved can be of various sizes and shapes and may have to flow through complex fluidic systems that can include contractions, expansions, bends, separation or merging of channels, as well as valves and fits. The suspension flow through such channels can lead to clogging when particles block a cross-section of the channel and prevent further particles from being transported downstream [51]. The clogging of a system usually leads to process failure and will require unclogging or, in severe cases, replacement of the system. Both of these scenarios are time-consuming and costly. Therefore, being able to predict the parameters to avoid or at least limit clogging in different types of suspensions and fluid systems could lead to more resilient and sustainable systems [8].

A critical challenge in estimating the clogging probability or the lifetime of a system

is that different clogging mechanisms can be simultaneously involved in the blockage of the channels [4, 8]. Besides, different length scales are present in the system. Usually, one needs to consider a characteristic particle size, such as its diameter d and the width of the constriction W. Small colloidal particles ($d \ll W$) with attractive interactions between themselves and the channel walls can form successive layers that clog a channel by aggregation [52, 53, 54, 55, 56, 57]. When the particles are smaller but of the same order of magnitude as W, stable arches can form at constrictions leading to clogging by bridging [11, 12, 58, 59, 60, 61]. Lastly, clogging by sieving has been reported at constrictions when the size of the particles d is larger than the constriction width W [10]. This clogging mechanism is usually straightforward to predict with rigid spherical particles but is more challenging to capture for complex particles. For instance, past studies have reported that deformable particles such as protein aggregates [19] and gel beads [13] may clog because they are larger than the constriction. Nevertheless, increasing the driving pressure leads to the deformation of the particles, which can then squeeze through the constriction and thus do not clog the channel [62, 63].

Most studies investigating clogging have considered spherical particles. However, many practical processes, especially in extrusion-based additive manufacturing, use suspensions of anisotropic particles. For instance, the addition of fibers to a matrix can improve the physical properties of the final material [64, 65, 66]. An issue in predicting the clogging in the dispensing system is that the geometry of the fibers introduces two length scales: their length L and diameter d. Since the length of the fiber L can be quite large compared to W, fiber suspensions are prone to clog the system, especially at the nozzle. Indeed, the nozzle constitutes a constriction, and in situ X-ray radiography and X-ray computed tomography studies have shown that clogging is often caused by the pileup of misoriented fibers near the nozzle tip [67, 68]. The clogging can also be triggered by the accumulation of misoriented fibers at reductions in the channel cross-section

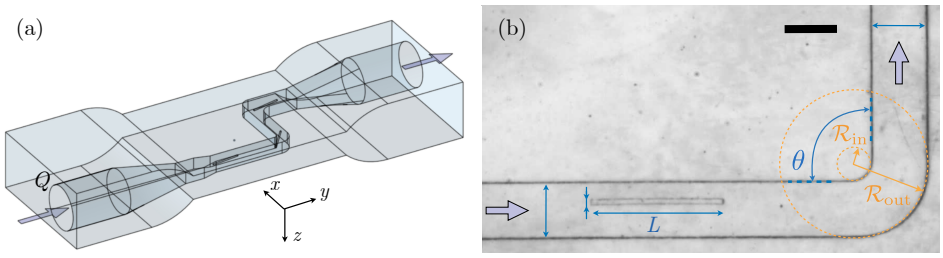

Figure 3.1: (a) 3D computer-aided design (CAD) rendering and (b) top picture of an example of millifluidic channel of constant width W with a fiber flowing from left to right. The arrows indicate the flow direction. The flow is driven at constant flow rate Q, and rigid fibers of diameter d and length L flow through the bent of angle θ, and of outer (resp. inner) radius of curvature $\mathcal{R}_{\text{out}}$ (resp. $\mathcal{R}_{\text{in}}$). The scale bar is 1.5 mm.

[69, 70]. At a different scale, such geometry is found in the transport of log jams that can accumulate in rivers and lead to floodings [71, 72].

One challenge in describing the clogging of a fiber in a channel is the difficulty, compared to a spherical particle, in modeling its motion. Since the aspect ratio of a fiber, *i.e.*, the ratio of its length to its diameter $\alpha = L/D$, is usually large, classical approaches to describe the transport of a fiber rely on the slender body theory [73, 74, 75]. Past studies have usually considered the transport of rigid and flexible fibers, for instance, during the sedimentation of the fiber in an unbounded fluid or in the vicinity of a wall [76, 77, 78]. Pressure-driven flows of rigid fibers and flexible filaments introduces subtleties such as cross-streamline migration and depletion near the channel walls [79, 80, 81]. Analogous experimental approaches have often relied on microfluidic systems. For instance, Berthet *et al.* have investigated the transport of free fibers in straight microchannels and, in particular, the evolution of its orientation [82]. The influence of straight walls has been investigated in confined channels and exhibited different peculiar dynamics [83]. The possible flexibility of the fibers introduces additional complexity since now one needs to account for the possible deformation of the slender fiber and its resulting dynamics [84, 85, 86, 81].

Whereas the possible sieving of particles in a channel has been described for spherical

particles, the situation remains less clear for the transport of fibers. In particular, whereas most studies devoted to the clogging of suspension have considered the presence of a constriction, other geometrical changes are present in a channel. For instance, a recent numerical study has considered the flow of a dense suspension of particles at the bend of a channel of constant cross-section [87]. Such geometry is quite common in practical systems since the tubings need to connect different parts and cannot only be straight. One issue when considering the transport of fibers in such geometry is that the fiber needs to rotate at the bend to pass. Therefore, even if the diameter of the fiber is small, a long fiber may not be able to reorient itself and could clog the elbow. Being able to predict the critical parameters for which a fiber suspension will clog an elbow is important in dispensing systems, but the role of the different parameters remains elusive. In this chapter, we consider the probability of clogging for a rigid fiber flowing through a bent millifluidic channel. In particular, we aim to characterize the role of the length of the fiber, the width of the channel, and the radius of curvature on the clogging dynamics.

We first present in section 3.2 the experimental and numerical methods used in the following. We then report the different possible dynamics observed when varying the experimental parameters in section 3.3, and we established the evolution of the probability of clogging of the fibers at the bent. We then consider a geometrical model that predicts the limit case for which the fiber clogs the channel, and we further demonstrate that the evolution of the probability of clogging is also linked to the probability distribution of the position of the fibers in the channel upstream of the bend. Our results provide some guidelines for designing fluid systems for the transport of fiber suspensions resilient to clogging.

3.2 Methodology

3.2.1 Experimental Methods

The millifluidic devices used in this study are obtained using a stereolithography printing method (Formlabs, Form 3). For more details, see Ref. [59]. The geometry of each device is first designed with a Computer-Aided Design (CAD) software, as shown in the rendering in Figure 3.1(a). For all devices, the channel consists of three parts. First, a narrowing section allows us to connect the inlet with a circular section to the rectangular channel. Second, the channel consists of a rectangular section of height H and width W. In this section, we add a bend of angle 90° and of outer (resp. inner) radius of curvature $\mathcal{R}_{\text{out}}$ (resp. $\mathcal{R}_{\text{in}}$). This part of the channel is our region of interest in this study and is shown in figure 3.1(b). Finally, another narrowing section connects the rectangular channel with the circular outlet. We designed the rectangular channel with an upstream and downstream part that is sufficiently long to neglect the influence of the narrowing section on the flow in the main channel (*i.e.,* longer than the entry length).

The height of the channel is kept constant and equal to $H = 1.55 \pm 0.15\,\text{mm}$ along the entire rectangular channel. This value of H allows us to neglect vertical confinement effects on the fibers since their diameter is much smaller than H. Each channel is characterized by two parameters: the channel width W and the radius of curvature of the outer wall $\mathcal{R}_{\text{out}}$ (see figure 3.1(b)). Note that the radius of curvature of the inner wall is simply given by $\mathcal{R}_{\text{in}} = \mathcal{R}_{\text{out}} - W$. Thanks to the tune-able manufacturing method of the devices, we can change these parameters independently.

The dilute suspensions consist of non-Brownian fibers dispersed in a Newtonian interstitial fluid. The fluid used in our experiments is a mixture of polyethylene glycol (PEG with an average molecular weight of 3,900g, from Sigma Aldrich), DI water, and zinc chloride ($ZnCl_2$, from Sigma Aldrich) at the mass fraction of 0.35, 0.55, and 0.10,

Geometry	# 1	# 2	# 3	# 4	# 5
W	1.5 mm	1.5 mm	1.5 mm	1 mm	2mm
$\mathcal{R}_{\text{out}}$	2 mm	1.5 mm	4 mm	2 mm	2mm

Table 3.1: Geometrical parameters used in the different geometries of the bent channels considered in this study.

respectively. The density is measured with an Anton Paar DMA 35 densimeter and is equal to $\rho = 1.1342\,\text{g.cm}^{-3}$. This density was chosen to be close to the density of the fiber so that the suspension can be considered as neutrally buoyant over the timescale of the experiments. The dynamic viscosity of the interstitial fluid has been measured with a rheometer equipped with a cone-plate geometry (Anton Paar MCR302) and is equal to $\eta = 156\,\text{mPa.s}$.

The fibers are made from nylon wires of diameters $d = 120\,\mu\text{m}$ and $d = 200\,\mu\text{m}$. These wires are cut into small fibers of different lengths ranging from $L = 1.5\,\text{mm}$ to $L = 6.5\,\text{mm}$. The resulting aspect ratio of the fibers, L/d is thus between 7.5 and 54. The density of nylon fiber is $\rho \simeq 1.13\,\text{g.cm}^{-3}$, close to the density of the interstitial fluid.

We considered two flow rates in our experiments, $Q = 0.4\,\text{mL.min}^{-1}$ and $1.6\,\text{mL.min}^{-1}$. The elasto-viscous number is defined as $\text{Sp} = 16\,\eta\,U\,L^4/(d^4\,E)$, where U is the flow velocity, E the Young's modulus of the nylon wire, and $\dot{\gamma} = U/L$ the shear rate. In the present situation, $E \sim 1 - 3\,\text{GPa}$, $U \sim 3.0\,\text{m.s}^{-1}$, so that $\text{Sp} \ll 1$ for all experiments performed in this study. We also visually checked possible deformations of the fibers in the channel for several flow rates. For the flow rates used here, the fibers do not exhibit any visible deformation, and we can thus approximate that the fibers used behave like rigid rods.

The values of the flow rate also lead to a laminar flow inside the square channel since the associated Reynolds number is of order 0.1. Therefore, inertial effects can be neglected compared to viscous ones, and the flow in the channel can be assumed to be

purely viscous.

The experimental setup consists of a syringe filled with the fiber suspension, placed in a syringe pump (KDS Legato 110) that drives the flow in the device at a constant flow rate Q. The syringe is connected to the millifluidic device using 3.2mm inner diameter plastic tubings. The system is backlit using an LED panel (Phlox) to enhance the contrast and ease the processing of the experiments. The flow and the fiber dynamics in the channel are captured using a CMOS camera (FlowSense) at 40 fps and a resolution of 68.4 pixels/mm. The suspension is delivered with a continuous flow, and once a fiber is about 5 cm upstream of the entrance of the millifluidic device, we trigger the recording. The suspension is dilute enough so that the fibers arrive one by one inside the channel, as illustrated in figure 3.1(a), and we can focus on the clogging probability of a lone fiber with no interactions with others.

As fibers are often longer than the inner diameter of the connective elements used to link tubing, clogging at the connectors became an issue for some of the trials, resulting in a loss of control over flow rate, blockages where individual fibers could no longer reach the test section, and most significantly, an inability to isolate individual fibers in the test section. To address this issue, for certain trials, the experimental setup was modified slightly to recycle individual fibers through the system using a parallel path connected to a hand-controlled syringe. This was found to be an effective method for accelerating experimentation and isolating individual fibers in cases where the fibers were so long that they regularly clogged and formed aggregates in connectors or inside of the syringe containing the suspension.

Theoretically, a fiber is considered clogged if it does not move for an infinite time. Experimentally, we define a time after which a fiber that stopped at the bent can be considered definitively clogged. We consider in the following that the channel is clogged if a fiber is stuck at the bend for more than 5 seconds, which nearly corresponds to the

time taken by a fiber to cross the main channel of the channel. The channel height H is comparable to the channel width. As a result, a fiber can slightly tilt. We, therefore, assimilate the apparent length of the fiber to their length. The apparent length corresponds to the projection of the fiber length on the $x - y$ plane.

The detection and tracking of the fibers in the channel are performed using a custom-made ImageJ macro. Each video is binarized, and the coordinates of the channel walls are recorded. Then, the first frame is subtracted from the full video, and the noise is reduced to obtain only the fiber in the images. We then measure the apparent fiber length, its position in the channel, and its orientation, 2 mm upstream from the bend. The orientation is characterized by an angle φ between the axis of the fiber and the direction of the channel. We can also track the fibers during this entire process to measure the time evolution of their position and their orientation along the channel. We finally characterize whether the fiber clogged the channel or not.

3.2.2 Numerical Methods

[Numerical Methods section by Harishankar Manikantan and Thomas Nguyen.]

We will compare experimental observations of free transport versus clogging of rods via a simplified model of fiber-fluid interactions and wall friction. We model the fibers of aspect ratio $\epsilon = d/2L$ as rigid rods parameterized by the arc length $s \in [-L/2, L/2]$ such that $\mathbf{x}(s,t) = (x(s,t), y(s,t))$ describes its centerline coordinates. The position of any point along the rod's centerline can be written as $\mathbf{x} = \mathbf{x}_0 + s\hat{\mathbf{p}}$, where $\mathbf{x}_0$ is the fiber's center of mass (corresponding to $s = 0$), and $\hat{\mathbf{p}}$ is a unit tangent vector prescribing its orientation. Using a resistive force description for slender fibers in viscous flows

[74, 88, 89, 75], the centerline velocity of a rigid rod is

$$\dot{\mathbf{x}}_0 + s\dot{\hat{\mathbf{p}}} - \mathbf{U}_0\left(\mathbf{x} + s\hat{\mathbf{p}}\right) = \frac{\ln \epsilon}{4\pi\eta}\left(\mathbf{I} + \hat{\mathbf{p}}\hat{\mathbf{p}}\right) \cdot \mathbf{f}\left(\mathbf{x} + s\hat{\mathbf{p}}\right). \tag{3.1}$$

Here, over-dots represent time derivatives so that $\dot{\mathbf{x}}_0$ is the fiber's translational velocity and $\dot{\hat{\mathbf{p}}}$ is its rotational velocity about the center of mass. $\mathbf{U}_0$ is the background fluid velocity and $\mathbf{f}$ is the force distribution acting on the fiber. The background fluid velocity corresponding to each experimental geometry is obtained via direct numerical simulation (COMSOL Mulitphysics). The simulation results are then interpolated into a third-order bivariate spline rectangular grid. In this simple local treatment, we ignore hydrodynamic interactions between parts of the fiber or between the fiber and the channel walls.

Fibers are freely suspended in the fluid unless they come into contact with a channel wall. Integrating Eq. (3.1) across the length of such a freely transported fiber and setting the total hydrodynamic force acting on the particle to zero gives its translational velocity:

$$\dot{\mathbf{x}}_0 = \frac{1}{L}\int_{-L/2}^{L/2} \mathbf{U}_0\left(\mathbf{x} + s\hat{\mathbf{p}}\right)\, \mathrm{ds}. \tag{3.2}$$

Similarly, integrating the first moment of Eq. (3.1) with s and requiring that the net torque on a freely suspended fiber be zero yields, after some manipulations [75, 74],

$$\dot{\hat{\mathbf{p}}} = \frac{12}{L^3}\left(\mathbf{I} - \hat{\mathbf{p}}\hat{\mathbf{p}}\right) \cdot \int_{-L/2}^{L/2} s\mathbf{U}_0\left(\mathbf{x} + s\hat{\mathbf{p}}\right)\, \mathrm{ds}. \tag{3.3}$$

With $\mathbf{U}_0$ fully known across an Eulerian grid and interpolated onto a discretized Lagrangian representation of the fiber, the time evolution of a fiber's center and orientation can be determined by numerically integrating Eqs. (3.2)–(3.3). The full fiber is then reconstructed as $\mathbf{x} = \mathbf{x}_0 + s\hat{\mathbf{p}}$.

The governing equations for translational and rotational dynamics change when the

fiber makes contact with a wall. We lump contact forces into discrete point forces $\mathbf{F}_i$ at one or more points parametrized as $s = \lambda^i$ along the rod that are activated when parts of the fiber are within, Δ, a threshold distance from a wall. More generally, lubrication effects influence the close approach. For this work, we do not seek to model details of the near-field hydrodynamics but instead, lump such contact interactions into a simplified solid-solid friction model. As the net force on a fiber during wall contact is non-zero, integration of Eq. (3.1) and its first moment now gives [75, 74] modified expressions of translational and rotational velocity of the center of mass:

$$\dot{\mathbf{x}}_0 = \frac{1}{L}\int_{-L/2}^{L/2} \mathbf{U}_0\left(\mathbf{x} + s\hat{\mathbf{p}}\right)\,\mathrm{ds} - \frac{\ln\epsilon}{4\pi\eta}\left(\mathbf{I} + \hat{\mathbf{p}}\hat{\mathbf{p}}\right)\cdot\sum_i \mathbf{F}_i. \tag{3.4a}$$

$$\dot{\hat{\mathbf{p}}} = \frac{12}{L^3}\left(\mathbf{I} - \hat{\mathbf{p}}\hat{\mathbf{p}}\right)\cdot\int_{-L/2}^{L/2} s\mathbf{U}_0\left(\mathbf{x} + s\hat{\mathbf{p}}\right)\,\mathrm{ds} - \frac{12}{L^3}\frac{\ln\epsilon}{4\pi\eta}\left(\mathbf{I} - \hat{\mathbf{p}}\hat{\mathbf{p}}\right)\cdot\sum_i \lambda^i\mathbf{F}_i. \tag{3.4b}$$

At the point of contact, we determine the unit tangent vectors and normal vectors, $\hat{\mathbf{t}}$ and $\hat{\mathbf{n}}$, respectively, along the channel walls near the point of contact. Note that $\hat{\mathbf{n}}$ is always pointed into the channel and away from the walls, whereas $\hat{\mathbf{t}}$ is pointed in the direction of flow. $\mathbf{F}_i$ is comprised of both a normal force that prevents rod penetration into the wall and a frictional force that either opposes the motion of the rod at the point of contact or prevents its movement about that point.

To determine $\mathbf{F}_i$, we first calculate the hydrodynamic force, $\mathbf{F}_{\text{flow}}$, that is experienced by the rod:

$$\mathbf{F}_{\text{flow}} = \int_{-L/2}^{L/2}\mathbf{f}(s)\,\mathrm{ds} = -\left(\frac{\ln\epsilon}{4\pi\eta}\right)^{-1}\left(\mathbf{I} - \frac{1}{2}\hat{\mathbf{p}}\hat{\mathbf{p}}\right)\cdot\int_{-L/2}^{L/2}\mathbf{U}_0\,\mathrm{ds}, \tag{3.5}$$

and then project it onto the unit normal and tangent vectors respectively:

$$\alpha = \mathbf{F}_{\text{flow}} \cdot \hat{\mathbf{n}} \tag{3.6a}$$

$$\beta = \mathbf{F}_{\text{flow}} \cdot \hat{\mathbf{t}} \tag{3.6b}$$

To estimate the frictional force, we apply a simple Coulomb friction model during contact between the fiber and the channel wall. More specifically, we determine if the hydrodynamic force in the tangential direction exceeds the static friction threshold:

$$|\beta| \leq \mu_s |\alpha| \tag{3.7}$$

Here, μ_s is the coefficient of static friction. If Equation 3.7 holds true, that means that the static friction of the wall is strong enough to prevent the rod from further sliding. To estimate this, we calculate $\mathbf{u}_c$, the velocity of the point of contact on the rod as if it were freely-floating [74]:

$$\mathbf{u}_c = \dot{\mathbf{x}}_0 + \lambda^i \dot{\hat{\mathbf{p}}} \tag{3.8}$$

We time-march the rod's position using Equations 3.4a and 3.4b, and then correct for the rod's position with $\mathbf{u}_c$ to effectively "pin" the rod about that point.

During instances where the rod is sliding along the wall (i.e.: Equation 3.7 does not holds true), we adapt from the contact algorithm from previous works [90, 81, 85]. $\mathbf{F}_i$ is of the following form during these instances:

$$\mathbf{F}_i(s) = -\mu_k |\alpha| \hat{\mathbf{t}} + F_R \hat{\mathbf{n}}, \tag{3.9}$$

where μ_k is the coefficient of kinetic friction, and F_R is the steric repulsion force required

to prevent rod penetration into the walls. To determine F_R, we first calculate d, the absolute distance between each rod point and the closest point along the wall. F_R is then determined by the following:

$$F_R(s) = \max\left[|\alpha|, |\left(1 - \left(\frac{\Delta}{2d}\right)^m\right)\alpha|\right] \tag{3.10}$$

Equation 3.10 is written such that the magnitude of F_R is at its maximum when $d \leq \Delta/2$, and thus acts to push the rod away from the walls. When $\Delta/2 \leq d \leq \Delta$, the repulsion force is comparable to the frictional force.

Our rod discretization, ds, was chosen to be $0.02 - 0.10$ mm. For our simulations, we choose $m = 8$ and $\Delta = 0.0375$ mm. dt, the time step to solve for the future rod position, was chosen to be 10^{-3} s; we adaptively reduce dt to 10^{-4} s should the rod come into close proximity with the flow geometry walls. In our simulations, there are two potential instances in which a rod could become clogged. A rod is determined to be "clogged" in our simulations if there are two or more points of contact where the rod is "pinned". A rod is also clogged if it is unable to past through the bend of the flow geometry in the same amount of time that it takes to travel vertically down the initial portion of the geometry.

3.3 Results

3.3.1 Phenomenology: Clogging or Not Clogging?

In our experiments with a fiber flowing past a 90° bend, we find that the sieving clogging mechanism best describes how the fibers clog. Using knowledge of the sieving mechanism, it can be concluded that if all of the fiber's characteristic dimensions (notably length) are less than the diameter of the tubing, fibers can be characterized as never

clogging, as seen in Figure 3.2(a). Experimentally, it was also observed that even slightly larger rigid fibers ($L_{fiber} > D_{tube}$) tend not to clog the channel if they do not make contact with at least two different points on the channel walls, as they never develop a sufficient frictional interface to resist the drag force within the channel. Although it is hard to conclusively predict whether any one fiber will satisfy such a condition, the experimental probability of avoiding two points of contact decreases with increasing fiber length and initial fiber position x_c.

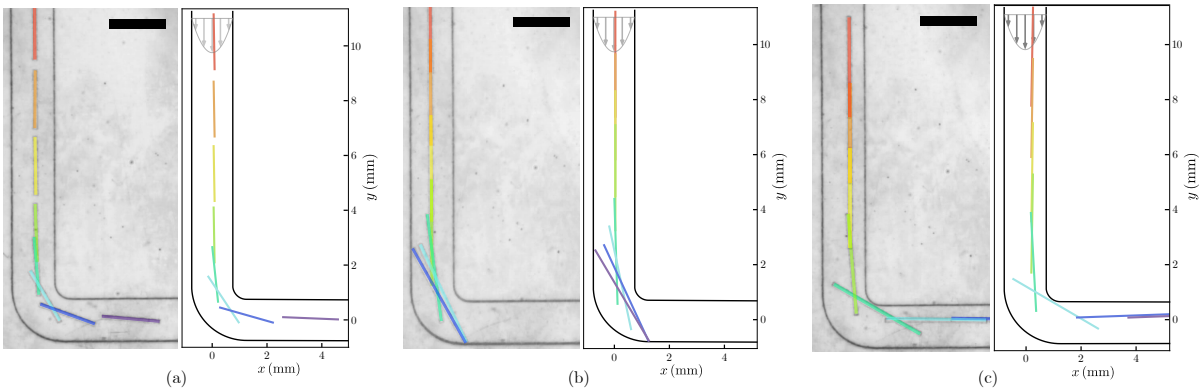

Figure 3.2: Examples of experimental (left) and numerical (right) behavior observed for a fiber flowing through a bend. (a) Below a threshold length, a fiber can reorient without touching the channel walls and flow through the bent ($L = 2\,\text{mm}$). (b) Beyond a threshold length, the fibers can get clogged at the bent by making contact with the channel walls ($L = 3.8\,\text{mm}$). (c) A long fiber that would clog when flowing at the center of the channel can reorient and flow through if it is close enough to the inner wall ($L = 3.5\,\text{mm}$). Scale bars are 2 mm, the flow goes from top to right, and the time goes from red to purple.

An opposite behavior is observed for very long fibers, beyond a certain threshold length; in this case, when the fiber approaches the bend and starts to reorient itself, the leading end of the fiber will touch the channel walls at two locations (Figure 3.2(b)). Even if we consider a slip boundary condition at the surface, a sufficiently long fiber will keep rotating until eventually touching the the channel walls at three different points: two contact points on the outer walls upstream and downstream from the bend and a third contact on the inner wall in the bend. Such long fibers do not have sufficient space

to orient parallel to the streamlines exiting from the bend and as a result remain stuck in the channel.

Between these two regimes, the fibers display more complex dynamics; for moderately long fibers, the fiber can collide with the walls at two locations, but because of its size, it either "slips" along the walls (Figure 3.2(c)) or "sticks" onto them. The dynamics of fibers in this regime are due to a competition between the external flow field that transports the fiber through the flow geometry and past the bend, and frictional contact/viscous drag forces that aim to hinder and change the fiber's trajectory. Because of random variations in fiber position and orientation at the bend, it is nearly impossible to predict clogging for any individual fiber in this regime without knowing its position and orientation at the bend, however, we can use statistical models to make general predictions of fiber behaviors.

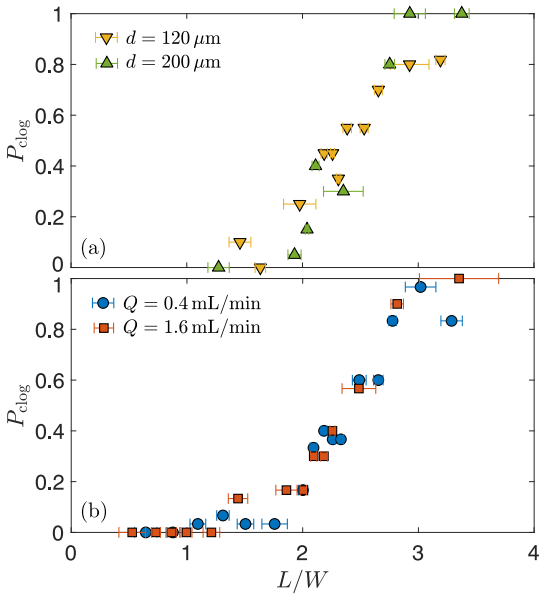

Figure 3.3: Clogging probability P_{clog} as a function of the normalized fiber length L/W in the geometry #1 for (a) two different fiber diameters ($d = 120\,\mu m$ and $d = 200\,\mu m$) and a flow rate $Q = 0.4\,\text{mL.min}^{-1}$. Each data point represents the probability for 20 fibers. (b) Comparison of the clogging probability for two different flow rates ($Q = 0.4\,\text{mL.min}^{-1}$ and $Q = 1.6\,\text{mL.min}^{-1}$). Each data point represents 30 fibers. Error bars represent 1 standard deviation.

Overall, the simulations are able to capture the three different behaviors of "no clog", "clog", and "slip" observed in our experiments. For some fiber lengths, we observe one or two behaviors, and for the others, we observe all three. This suggests that the probability of clogging in some cases are neither zero nor unity. However, the probability of clogging could potentially be dependent on both the size of the fiber or the background flow rate. To investigate this, we use geometry #1 with flow rates of $Q = 0.4\,\mathrm{mL.min^{-1}}$ or $Q = 1.6\,\mathrm{mL.min^{-1}}$, and allow fibers with a diameter of $d = 120\,\mu\mathrm{m}$ and $d = 200\,\mu\mathrm{m}$ to flow through. We then perform image processing analysis on our experimental data and plot the probability of clogging in Geometry #1 based on the fiber's length (Figure 3.3).

For the two fiber diameters that we studied, we observe that the tendency of a fiber to clog does not seem to depend significantly on the diameter (Figure 3.3 (a)). As we increase the fiber's length, the probability of clogging monotonically increases from zero to one, with no strong differences between the probability curve between the two different diameters. Therefore, for the two diameters considered in this study, the influence of fibers diameter can be neglected.

With our chosen flow rates of $Q = 0.4\,\mathrm{mL.min^{-1}}$ or $Q = 1.6\,\mathrm{mL.min^{-1}}$, this leads to Reynolds numbers of $\mathrm{Re} = 0.034$ and $\mathrm{Re} = 0.135$, respectively, allowing the fiber to stay in Stokes flow. With these flow rates, we do not observe any noticeable differences on their effects of the fiber probability curves(Figure 3.3(b)). Moreover, the flow rates do not seem to significantly affect the fiber position distribution in the channel (see supplementary materials). As a result, we use a flow rate of $0.4\,\mathrm{mL.min^{-1}}$ for the rest of our study. We should emphasize that it would be interesting to study how the clogging probability evolves at larger Reynolds numbers, in particular when inertial effects would come into play. However, these effects are beyond the scope of the present study that is restricted to viscous flows.

These probability curves also show the three distinct behaviors previously described

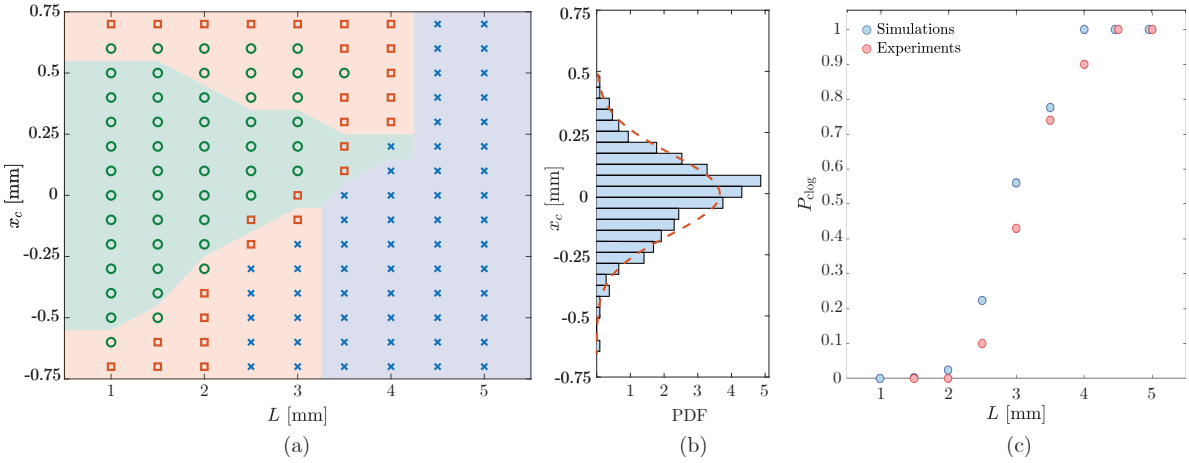

Figure 3.4: (a) Phase diagram showing the outcome of an initially vertical fiber's motion at the bend. The symbols are experimental data for "Clog" indicates that the fiber is stuck inside the bend (blue crosses), "Free" indicates that the fiber does not come into contact with the walls in the bend at all (green circles) and "Contact" with walls but sometimes clogs and sometimes does not clog (orange squares). The shaded area are the numerical domains. Simulations were run using friction coefficients of $\mu_k = 0.85$ and $\mu_s = 0.60$. (b) PDF of the position of the center-of-mass of the fiber extracted 2.0 mm upstream of the bent in the channel geometry #1 ($W = 1.5$ mm, $\theta = 90°$, and $\mathcal{R}_{\text{out}} = 2$ mm). The dashed line shows the best fit using a normal distribution. (c) Resulting clogging probability P_{clog} as a function of the fiber length L/W in the geometry #2.

for our experimental and simulation data. First, for small lengths ($L/W < 1.8$), the clogging probability, P_{clog} is close to zero. As a consequence of their high aspect ratio, most fibers considered in this study tended to reorient parallel to the streamlines when flowing around the bend if they had enough space to do so. At values $L/W < 1.8$, there was sufficient space for reorientation, and in turn, a very low clogging probability.

In the second regime, long fibers, here $L/W > 3.5$, are seen to clog at a probability $P_{\text{clog}} = 1$. In this case, fibers are longer than the maximum length of fibers allowed to pass through the bend; therefore even with a completely frictionless interface, their long lengths relative to the width of the channel prevent them from flowing past the bend. Later, we will discuss the bounds of fiber lengths beyond which fibers must always clog.

A transition regime between the two previous behaviors can also be seen, where the

clogging probability monotonically increases from $P_{\text{clog}} = 0$ to $P_{\text{clog}} = 1$. This transition regime is the most complex to explain as it depends on the fiber behavior in the channel; in our experiments, it is hard for two fibers to behave exactly the same due to the randomness of initial fiber position and orientation. Thus, the following sections in this chapter will focus on discussing important fiber and geometry parameters that lead to clogging. Then we will create a model that accounts for these characteristics, thus leading to a prediction of whether the fiber will clog or not in this sieving regime.

3.3.2 Clogging Probability in the Bent Channel

To determine which fiber characteristics lead to clogging, we first examine the fiber's orientation angle, φ, and x-center of mass position, x_c, where $x_c = 0$ corresponds to the outer wall, and $x_c = W$ corresponds to the inner wall. From examining these values prior to the flow bend in our flow geometry, we can determine the range of these parameter values that lead to clogging in various scenarios. Figure 3.5 shows the distribution of x_c and φ values that either lead to clogging or no clogging. We find that a clogging event strongly depends on the position of the fiber within the channel. The distribution associated with clogged fibers is shifted towards larger values of x_c, and centered around $x_c/W = 0.54$ (Figure 3.5(a)). Conversely, fibers that do not clog have a higher tendency to be located towards the inner wall. The distribution associated to these last fibers is centered around a smaller value $x_c/W = 0.47$.

The role of the fiber's orientation on its ability to clog is less obvious. In Figure 3.5(b), we can see that both distribution associated to clogged and not clogged fibers are similar. We find that the distribution of fibers orientation upstream from the bent section is narrow for both cases, suggesting that the fibers remain mostly parallel to the streamlines prior to the bend as expected. For different and more complicated geometries with less

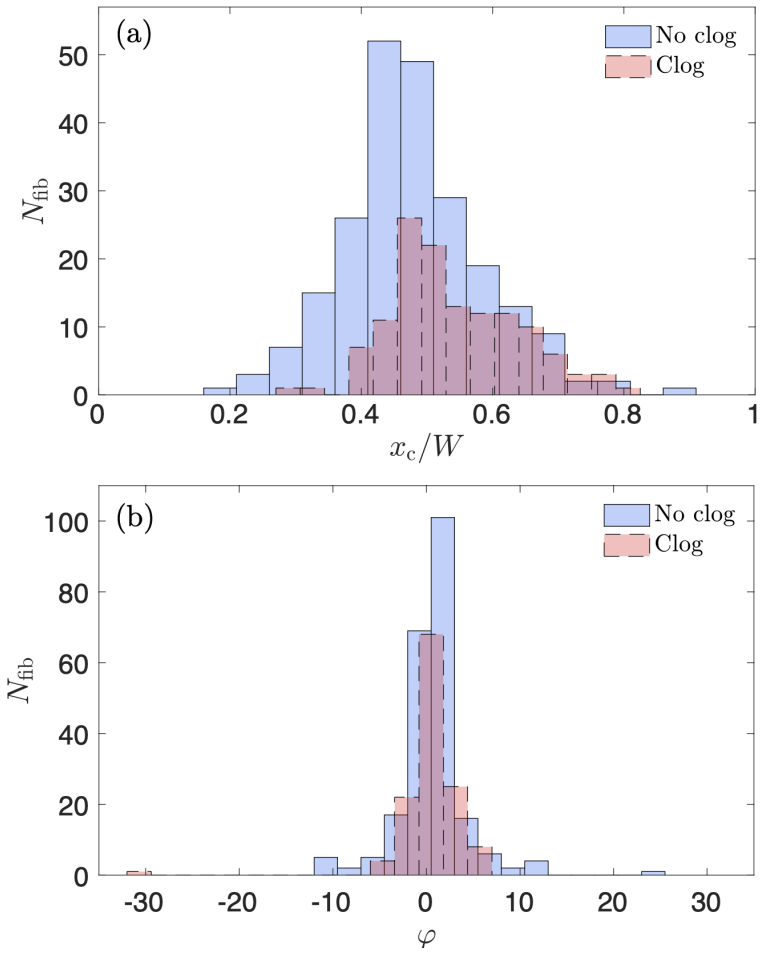

Figure 3.5: Distribution of (a) the position of the fiber center-of-mass x_c and (b) of the orientation of the fiber φ. The measurements are performed 2.0 mm upstream from the bent section. Fibers that lead to a clogging or no clogging event are represented in red or blue, respectively. The fiber length ranges here from 1.65 mm to 5.2mm and flowing in the geometry #1 ($W = 1.5\,\mathrm{mm}$, $\theta = 90°$, and $\mathcal{R}_{\mathrm{out}} = 2\,\mathrm{mm}$).

prevalent areas of unidirectional flow, We can expect a broader distribution of φ.

Figure 3.6 shows the evolution of φ as the fiber attempts to move past a flow bend angle of $\theta = 90°$. We find in our experiments that a fiber has to rotate more than 45° in order to pass through the bend, even during contact with the wall. Short fibers have an easier time rotating in the flow bend compared to long fibers, suggesting that fiber lengths affect its ability to clog. Therefore, we also assume that that there is a threshold

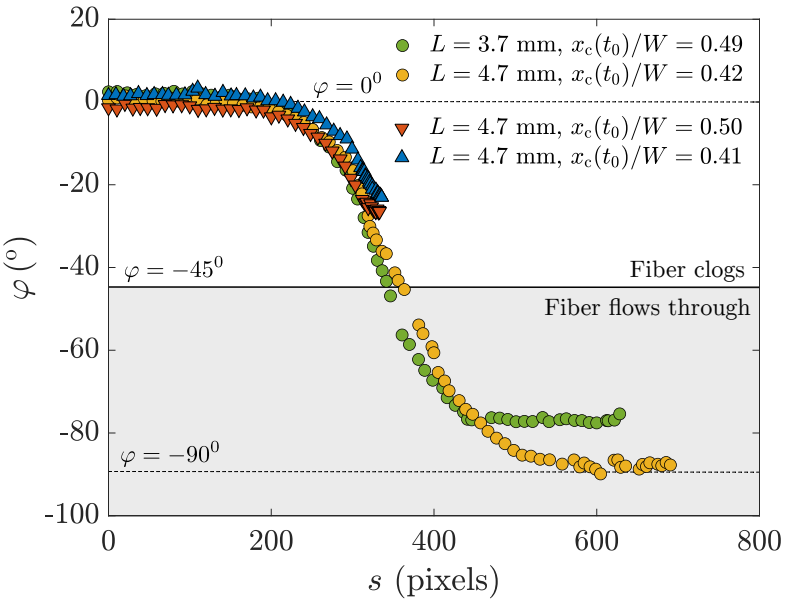

Figure 3.6: Example of the evolution of the orientation of the fiber with the vertical direction in the geometry #1. Initially, the fibers are aligned with the flow ($\varphi = 0°$) before rotating when approaching the bent. If the fibers are able to reorient more than $|\varphi| = 45^o$ they are able to flow through and slowly align themselves with the flow at the outlet ($|\varphi| = 90°$). Here, the red and blue triangles are two experiments where the fibers clogged, whereas the yellow and green flow through. s denotes the curvilinear coordinates along a streamline.

fiber length that determines whether a fiber becomes clogged or not.

3.3.3 Influence of Channel Geometry

As a fiber attempts to pass through the channel bend, the ratio of length to channel width, L/W, is a key parameter in determining if there is sufficient space for the fiber to reorient. However, the exact effect on clogging probability correlating with changes in channel width is not fully understood. To test the influence of channel width, experiments were conducted with 3 channel geometries, each with a 2 mm radius of curvature but varying widths. Each channel geometry was tested with fibers ranging from 1.5 mm to 6 mm, and for each length tested, a clogging probability was developed, defined as the

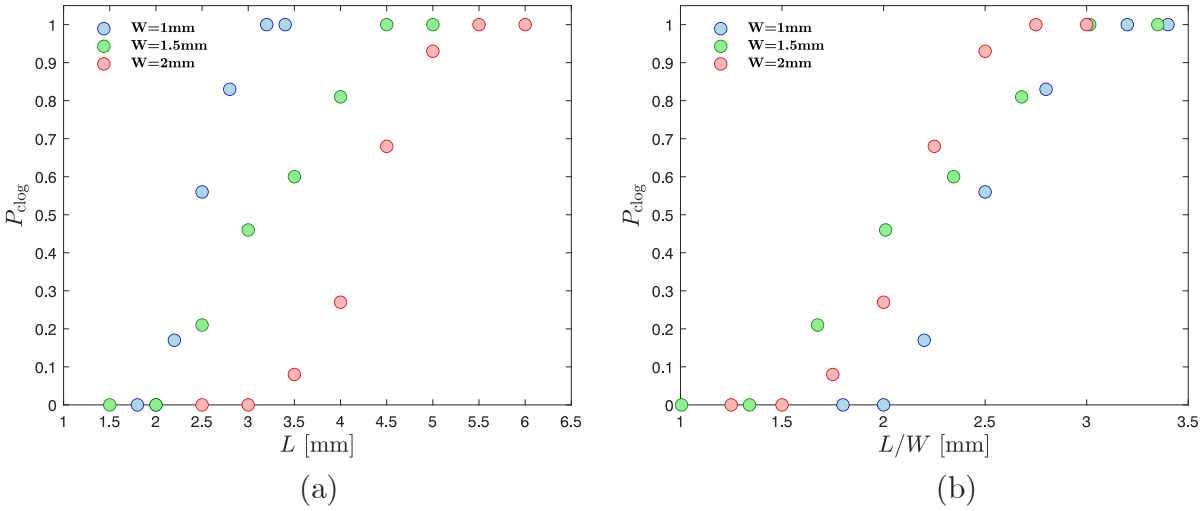

Figure 3.7: Clogging probability for fiber lengths between 1.5 mm and 6 mm travelling around a 90 degree bend. (a) Raw data. (b) Data normalized by channel width. Three geometries are used, each with a constant bend radius of 2 mm and varying channel widths. Blue represents 1 mm channel width, pink represents 1.5 mm channel width, cyan represents 2 mm channel width. A sample size of 30 trials is used for each data point to determine clogging probability.

number of clogs divided by the number of trials.

Figure 3.7 shows that there is a strong influence of channel width on the fiber clogging behavior. Increasing the channel width from 1 mm to 1.5 mm resulted in the maximum passing fiber length increasing from 2.7 mm to 4 mm; similarly, a further increase to 2 mm width resulted in fibers up to 5 mm long passing through the bend. Interestingly, the ratio L/W of the sieving threshold fiber length saw a very slight decrease with increasing width, initially at 3.2 for the shortest width, then 3.0, and 2.8 for the widest channel; this is consistent with the theory that channel bend radius is a limiting factor in fiber transport, even when the channel width is increased substantially.

Another noteworthy parameter is the radius of curvature at the bend; in theory, a larger radius of curvature should give fibers more space to reorient themselves and successfully pass through the bend without clogging the channel or forming a significant frictional interface with the walls. To develop a further understanding of the effect of

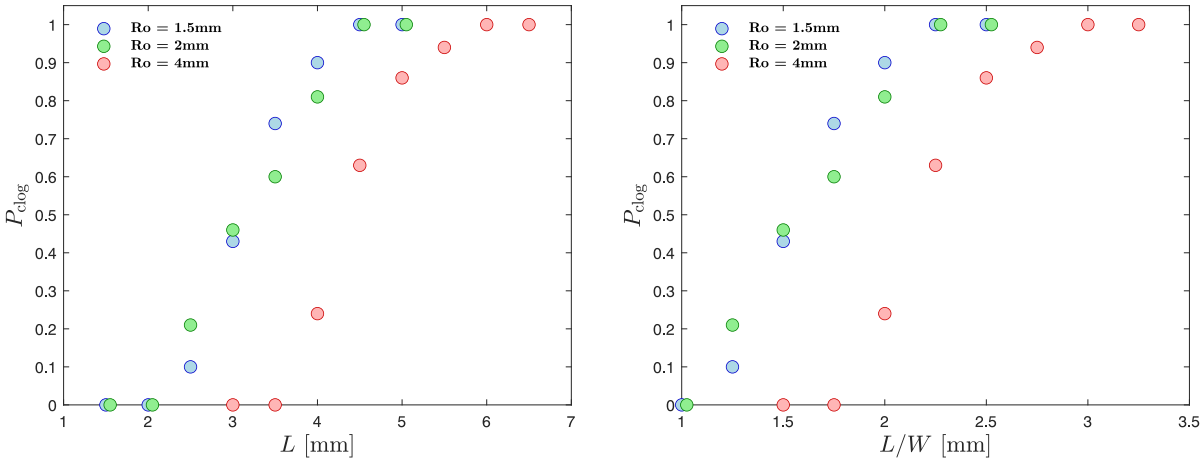

Figure 3.8: Clogging probability for fiber lengths between 1.5 mm and 6.5 mm traveling around a 90 degree bend. (a) Raw data. (b) Data normalized by channel width. Three geometries are shown, each with a constant channel width of 2 mm and varying bend radius. Blue represents 1.5 mm bend radius, pink represents 2 mm bend radius, cyan represents 4 mm bend radius. A sample size of 30 trials is used for each data point to determine the clogging probability.

the radius of curvature, clogging experiments were conducted with a channel width held constant at 1.5 mm and three different values of $\mathcal{R}_{\text{out}}$: 1.5 mm, 2 mm, and 4 mm. Fiber length was varied between 1.5 mm and 6.5 mm for these experiments to develop a relationship between clogging probability and fiber length for each different geometry.

Figure 3.8 shows the relationship between the bend radius of the channel and clogging probability. Notably, the 4 mm bend radius had much lower clogging probabilities compared to the 1.5 mm and 2 mm geometries for the same fiber lengths. Additionally, fibers up to 5.5 mm in length were observed to pass through the 4 mm bend radius geometry, whereas the longest fiber able to pass through either of the other geometries without clogging was 4 mm. Interestingly, there was very little difference in the clogging behavior of the 1.5 mm and 2 mm outer radius channel geometries, with each having the same maximum passing length, and the same lengths of 0% clogging probability. Compared to 0.5 mm changes in the channel width, a 0.5 mm change in the bend radius appeared

to have a lower order effect.

3.3.4 Estimating the Threshold Fiber Lengths for Clogging

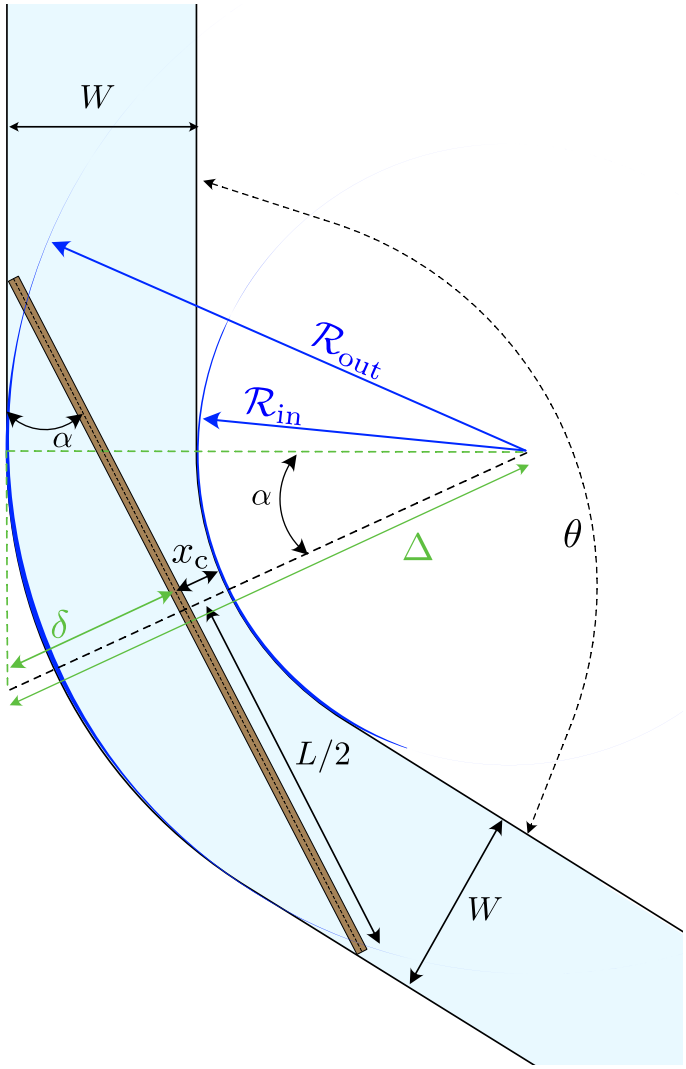

Figure 3.9: Schematics of a fiber of length L and diameter d flowing through the bent channel with radii of curvature $\mathcal{R}_{\text{out}}$ and $\mathcal{R}_{\text{out}}$, width W, and bend angle θ. The center of mass of the fiber is a distance x_c of the inner wall, and the fiber depicted here is at the onset of clogging.

Suppose a fiber attempting to move past the bent region of a flow geometry with an inner radius of $\mathcal{R}_{\text{in}}$, outer radius $\mathcal{R}_{\text{out}}$, bend angle θ, and width W (Figure 3.9). Its center

of mass is located x_c away from the inner wall ($x_c = 0$ and $x_c = W$ correspond to the inner wall and outer wall respectively). We define L_c as the threshold length that always leads to clogging. The geometrical constraints of the fiber in the flow geometry at the onset of clogging leads to several relationships: 1) the angle α is the orientation angle of the fiber and is related to the flow bend angle $\alpha = \pi/2 - \theta/2$, 2) Δ is the distance such that $\cos\alpha = \mathcal{R}_{\text{out}}/\Delta$, and 3) δ as the distance between the outer wall and the fiber's center of mass such that $\delta = \Delta - \mathcal{R}_{\text{in}} - x_c$. Combining these relationships leads us to an expression for L_c:

$$L_c = \frac{2\mathcal{R}_{\text{out}}}{\cos(\theta/2)}\left[1 - \sin(\theta/2)\left(1 - \frac{W - x_c}{\mathcal{R}_{\text{out}}}\right)\right]. \tag{3.11}$$

In particular, we can see that under our assumptions the longest fiber that can flow without clogging through a bent channel is obtained for $x_c \to 0$ and equals to:

$$L_c = \frac{2\,\mathcal{R}_{\text{out}}}{\cos(\theta/2)}\left[1 - \sin(\theta/2)\left(1 - \frac{W}{\mathcal{R}_{\text{out}}}\right)\right]. \tag{3.12}$$

Equation 3.11 applies for when the fiber makes contact with the inner wall. However, if the fiber is at a distance x_c larger than a threshold value x_c^*, the fiber will make contact at the outer curvature of the channel. In this case, the critical initial position for a fiber to clog is given by:

$$x_c^* = W - \mathcal{R}_{\text{out}}\left[1 - \sin\left(\frac{\theta}{2}\right)\right]. \tag{3.13}$$

For $x_c > x_c^*$, the threshold length for a fiber to make contact with the two boundaries in the curved part of the channel is:

$$L_c = 2\,\mathcal{R}_{\text{out}}\left[1 - \left(1 - \frac{W - x_c}{\mathcal{R}_{\text{out}}}\right)^2\right]^{1/2}. \tag{3.14}$$

The conditions described above account for the fiber touching the outer wall of the channel. However, we should emphasize that in this case, the friction at the wall may not be sufficient to hold the fiber in place, which may still flow through. These conditions are therefore different from a pure clogging condition.

3.4 Conclusion

Using a 3D printing method, we have been able to obtain millifluidic devices with different controlled geometries and study the behavior of an isolated neutrally buoyant and non-Brownian rigid fiber in different configurations. We have considered fibers of different lengths in each of these devices and have been able to characterize the probability of clogging as a function of the fiber length. We have shown that in small Reynolds number flows, the clogging of a bent channel by a rigid fiber is controlled by the geometry of the system, most importantly L/W and the initial position of the fiber x_c. We also extend our analysis through numerical simulations that describe the hydrodynamics of a slender rigid rod through slender-body theory. Our simulation results confirm our hypotheses regarding fiber clogging.

However, the clogging probability is not a simple step function going discontinuously from $P_{\text{clog}} = 0$ to $P_{\text{clog}} = 1$. We have identified three different regimes: (i) at small lengths compared to the width of the channel, the fibers have sufficient space to reorient while following a streamline without interacting with the channel walls. As a result, the clogging probability is $P_{\text{clog}} = 0$ in this regime. (ii) For very long fibers compared to the width of the channel, the bent section is too narrow, and the fibers stay stuck in the channel by being in contact with three points on the inner and outer walls. Even for frictionless particles, this situation always leads to a clogging event such that $P_{\text{clog}} = 1$. (iii) Between these two regimes, we have highlighted a transition regime for which the

fibers can flow through the bent section or clog depending on their length, their position in the channel, and their interaction with the lateral walls. In this regime, P_{clog} increases monotonically from 0 to 1, and the evolution depends on the friction at the wall. The boundaries between these three regimes shift with the geometry of the bent channel, characterized by its width W, its angle θ, and its inner and outer radii of curvature, $\mathcal{R}_{\text{in}}$ and $\mathcal{R}_{\text{out}}$.

The experimental results have been rationalized by a simulation that describes the clogging of a bent channel of a given geometry by a fiber of length L. To describe the evolution of the clogging probability with the different parameters, we have accounted for the distribution of the position of the center-of-mass of the fibers in the channel and the geometric condition. Using this technique, we were able to develop morphology diagrams and clogging probability data which can be used to predict fiber behavior for some scenarios; futhermore, this method could be applied to any scenario. Finally, for future improvement, the model needs to account for the possible sliding of the fibers on the sidewalls depending on the angle at which the fibers touch the wall.

The role of the friction and the possible sliding of the fibers will need to be considered in more detail in the future to improve the model. The role played by the apparent roughness of the device still needs to be better understood. A more extensive database varying θ, W and $\mathcal{R}_{\text{out}}$ will need to be obtained to get a better understanding of the influence of the channel geometry. Some hypotheses we have made in our model would also have to be compared to numerical simulations. For instance, the computation of the streamlines inside the bent section for a laminar flow, combined with a model of the transport of the fiber, would allow seeing if a rigid neutrally-buoyant fiber follows the same streamline when flowing through the bent section, and if at any time its orientation is tangential to the streamlines [75]. Understanding the clogging of a bent channel by rigid fibers is a first step towards understanding a variety of other clogging phenomena

involving fiber suspensions. For instance, a good comprehension of the influence of the channel geometry on the clogging event would allow us to better understand the clogging of porous media by small fibers. Indeed, streamlines going through a porous medium can be approximated by a succession of bent sections of different geometries and local radii of curvature. Knowing the role of the curvature, of the local width, and of the angle of each of these sections would enable us to model the clogging dynamics in media of a given porosity. For instance, this configuration could provide an estimate of how microplastics of elongated shapes can travel in soils.

Despite the hypotheses made, the present approach to studying the clogging of bent channel clogging by a rigid fiber paves the way to investigate additional complexity, such as the flow of flexible fibers. In particular, we expect that by considering various types of more or less flexible slender fibers, from polymeric rods to vegetal residues, we could account for the role of the flexibility in the clogging dynamics. In addition, manufacturing applications involve more or less concentrated suspensions of fibers, and the role of the collective motion at the bend on the clogging probability will have to be considered.

Chapter 4

Fluid Mechanics and Clogging in Drip Emitters

4.1 Introduction

Earth's growing population, combined with diminishing water resources, are expected to result in nearly six billion people suffering from clean water scarcity by 2050 [91]. Agricultural irrigation accounts for 70% of global water use, with a further 60% increase in projected by 2025 [92, 93]. Therefore, improving irrigation efficiency is a critical priority for maximizing clean water availability and increasing overall agricultural production. Drip irrigation, also known as micro-irrigation, can reduce the volume of water required by up to 70% when compared to sprinkler or furrow irrigation [94, 14], with a 20-90% increased crop yield [95, 96]. But only a small percentage of irrigated land uses drip systems [97]. This low adoption rate is due to the high maintenance demand of drip irrigation systems, which rely on small pores to deliver water to individual plants. One main issue is that the narrow channels in drip irrigation emitters can easily be clogged by suspended sediment, fertilizers, and biofilms like algae and bacteria. As a result, they

require continual monitoring and replacement [15, 98]. Therefore, clog mitigation is of paramount importance to improve the adoption rate of drip systems, saving water, and increasing crop yield.

In drip irrigation, the water is distributed through a pipe network and emitters at a low controlled discharge rate to each plant or adjacent to it [16]. Drip emitters, shown in figure 4.1(b), are the most important components of a system. The emitters are used to discharge the water from the pipe to the plants and control the quantity of water delivered. Different emitter arrangements on the pipe are possible; a widespread commercial method is integrating the emitter into the pipe at equally spaced intervals, corresponding with crop locations. Additionally, different types of drip emitters exist: pressure-compensating (PC) where each emitter has a pre-set flow rate, and non-pressure compensating (NPC) [99]. Whereas PC emitters incorporate a flexible membrane to regulate their resistance to flow [96], NPC emitters provide better longevity and lower maintenance thanks to the absence of any moving parts. Both types of emitters use long channels in the form of a labyrinth [100, 101]. The water flows from the pipe to the emitter, typically first through a lateral grid/filter that limits the entrance of large contaminants that could clog the channel of the emitter. The water then flows along a labyrinth path of varying length, on the order of 10 cm, with a cross-section on the order of a few millimeters square [Fig. 4.1(b), right]. This geometry is the most common one since it leads to a pressure drop in the form of head loss induced by the repetition of sudden changes in the flow direction [100, 102]. In NPC emitters, the evolution of the discharge rate Q and the pressure drop ΔP across the emitter is given by $Q = k\Delta P^{\alpha}$, where $\alpha \sim 0.3 - 0.8$ and k are constants that depend on the emitter design [103]. This relation governs the performance of the emitter and ensures a similar distribution of water between the emitters in the drip line. Many recent developments in emitter design focused on improving the labyrinth configuration, with respect to overall hydraulic performance

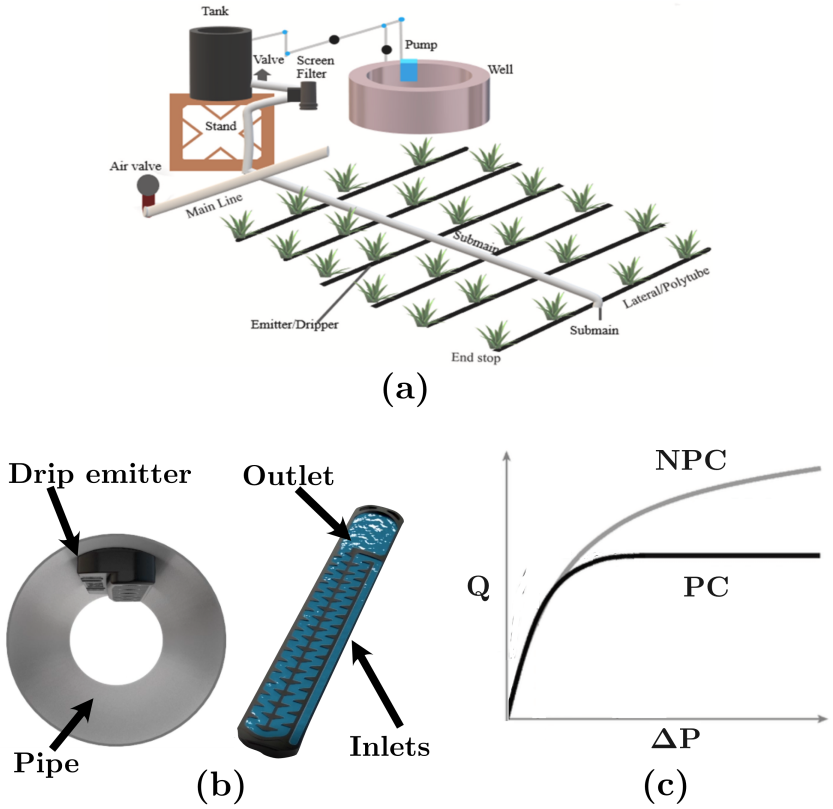

Figure 4.1: (a) Schematic view of a drip irrigation system [106]. (b) Left: Drip emitter in the main pipe. Right: Back view showing the labyrinth channel used to achieve the pressure drop. (source: Netafim) (c) Flow rate vs. pressure curves for flow across pressure compensating (top) and non-pressure compensating (bottom) drip emitters. [107]

and clogging characteristics [104, 105].

The large-scale deployment of drip-irrigation is limited by the decline of the discharge rate over time induced by the clogging of the emitters. Indeed, the narrow cross-sections and the constrictions are present in all emitters, making them susceptible to clogging. Given that clogging is the major cause of performance degradation, emitters are typically the main determinant of irrigation line life-time [98]. The problem of clogging can be produced by physical, biological and/or chemical causes. It is difficult and complex to determine the exact cause of emitter clogging, and the three forms of clogging can often

be observed simultaneously [108].

Physical Clogging

The primary mechanism of clogging in drip irrigation systems is physical clogging [15, 98, 99], however, there is variation in the clogging behavior depending on the type of particles suspended in irrigation water [109, 15]. Driven by the presence of physical particles, mainly sands, silts, and clays, this phenomenon occurs when particles become trapped in the channel, and over time, form aggregates with other particles flowing through the system [15, 14]. For larger particles, their clogging can be identified as a bridging mechanism; however, with smaller particles, clogging is mainly caused by an agglomeration effect where chemical bonds create large aggregates of sediments over long timescales [109, 110]. Often these effects can work together in real systems which have a mix of many particle types.

Biological Clogging

The second leading cause of clogging of drip-emitter is biological clogging; this mechanism is due to the presence of organic material in the water, especially in reclaimed water [111, 112]. The presence of organic matter leads to the formation of dense surface-dwelling communities, which begin to secrete an extracellular polymeric substance (EPS) that invades the cross-section of the microchannel, blocking downstream flow to crops [113].

Chemical Clogging

The presence of dissolved chemical elements in the water also has the potential to drive an alternate mechanism - chemical clogging. Depending on the temperature and the pH of the water, along with the salt concentration [114], chemical precipitation can occur within the drip-emitter channels. Although the effect is dependent on the particular chemical composition of the irrigation water being used, one common mechanism of chemical clogging is the formation of calcium carbonate inside of drip-emitters, which

can completely block the channel with solid matter [15].

In this review, we discuss the recent developments in drip irrigation technology, with respect to clogging performance. First, we discuss the relationship between drip emitter geometry and internal flow patterns. Additionally, the phenomena of physical clogging is examined in more depth, with focus on lab tests, small and large particle clogging. Finally, we discuss the current state of the art technologies and give an outlook to future improvements of reducing small particle clogging in drip emitters.

4.2 Geometry of Drip Emitters

The emitters are the most important component in drip irrigation systems. Indeed, they distribute water in controlled quantities as close as possible to the crop and are often the point of failure of drip irrigation systems. Drip emitters can mainly be categorized into two categories: on-line and in-line emitters. On-line emitters are typically attached externally to the irrigation pipes, allowing for flexible placement according to crop arrangements. They offer the advantage of customized dripper spacing but have the disadvantage of having to be installed manually [96]. In-line drip emitters are molded directly inside the pipe. They have the advantage of being cheaper, easier to set up in the field, and the benefit of providing a more uniform distribution of water, but the drawback is that they are installed at fixed intervals that cannot be changed [115].

In drip irrigation systems, emitters are strategically placed throughout irrigation lines, each one redirecting a small portion of the main channel flow through a constricting millifluidic channel consisting of a "labyrinth" pattern, before reaching an outlet at the base of a particular crop [99, 14]. This narrow and winding path within the emitter creates significant momentum losses through friction and turbulence, keeping the flow rate to crops relatively low, despite the high pressure driving the flow. In turn, a well-designed

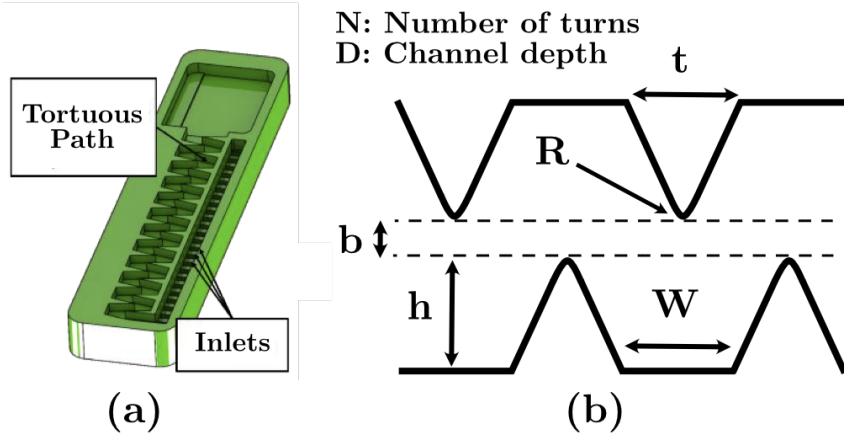

Figure 4.2: (a) Schematic of a drip emitter cross section, reproduced from Narain *et al.* [116] (b) Key geometrical parameters of drip emitter tortuous path designs. Tooth radius = R. Tooth offset = b. Tooth height = h. Tooth width = t. Tooth gap width = W. Number of tooth pairs = N. Channel depth = D.

drip emitter will minimize the coefficients k and α of the flow relation $Q = k\Delta P^{\alpha}$ [103]. Emitter channels are designed with careful consideration to ensure that their pressure drop is large enough to reduce flow rate, but not so large that it completely prevents flow. However, when particles become trapped inside the channel, the pressure drop increases above the nominal amount, causing the flow rate to decrease to undesired levels, or in extreme cases stall completely [15, 109]. As such, it is important to design emitters that create certain flow conditions which simultaneously mitigate the build-up of particles and proactively prevent clogging behavior.

In the majority of literature on drip irrigation, emitters are designed with alterations to the same key geometric parameters, based on the designs of most labyrinth emitters used in practice currently [117, 100, 116, 103]. Starting with a typical emitter labyrinth path like those commonly used in agriculture today, as seen in [Fig. 4.2], there are 7 key parameters which can be altered to influence flow behavior, and in turn, anti-clogging performance. Although there are of course more complex geometries possible, this simple pattern captures most of the common variations.

One consequential parameter to altering flow patterns in drip emitters is the tooth offset. As tooth offset is maximized, flow becomes concentrated in the center of the channel, creating a high velocity central flow and areas of relative stagnation in gaps between the teeth [117, 105]. Pressure drop is minimized and particles collected between teeth are relatively undisturbed by the flow. Conversely, as tooth offset is minimized, even below zero to where negative values are reached, the flow is forced to go around a series of bends, creating more turbulence and distributing kinetic energy more homogeneously throughout the channel [117, 105]. Pressure drop is maximized and particles collected between the teeth are subjected to turbulent flows. As such, it is typically desirable to minimize tooth offset to promote better anti-clogging performance.

Also noteworthy is the geometry of the teeth themselves, including width, height, radius, and gap width. The overarching principle with these parameters is that a tooth design which is larger relative to the channel, and less streamlined, will create more turbulence throughout the channel and create a larger pressure drop, similar to the effect of minimizing tooth offset [100, 117, 101]. However, there can be a variety of complex flow and particle deposition phenomena as a result of changing the angles and sizes of the internal features of the channel, some of which may be useful for improving anti-clogging performance. Another important parameter is the number of tooth pairs, a quantity which has a linear relationship with the pressure drop [100]. This parameter is especially interesting because it can be used to directly manipulate flow rate if other geometrical alterations used to address clogging have resulted in an undesirable irrigation flow rate.

Ultimately, the purpose of altering these parameters is to design an emitter which maintains a low flow rate while preventing particle deposition and aggregation within the emitter channel. However, it is important to discuss specifically what characteristics of the flow make this result possible. Some studies in emitter literature suggest that there is a relationship between quantity/size of vortex zones and the clogging behavior in emitters;

that is to say, by reducing the presence of low-velocity vortex zones, particle deposition is categorically reduced [118, 110]. Another important quantity is turbulent kinetic energy (TKE). Indeed, a study has shown that channels with smaller low-TKE zones and larger high-TKE zones had the best anti-clogging performance [118]. Despite the complexity and many variations of this two-phase clogging problem which often includes physical, biological, and chemical factors, the same concept remains across literature; emitter channels with well distributed flow and a high degree of turbulence seems to clog less and have the potential for the longest lifespan [104, 118, 110].

4.3 Physical Clogging Mechanisms

4.3.1 Experimental Tests

To develop robust drip emitter designs, it is crucial to test drip emitters for their anti-clogging performance under appropriate flow conditions, using suspensions of compositions that match irrigation water in the desired area of deployment. Laboratory tests of drip emitter clogging tend to take one of two forms: i) a rapid test (order of hours/days) where the goal is to achieve clogging as fast as possible with the aim of measuring the comparative anti-clogging performance of emitter designs [119, 120, 121] or ii) a long-duration test (order of weeks/months) meant to emulate real field conditions (or some aspect of real conditions) and predict the time evolution of practical performance of emitters [109, 110]. Both tests have their own unique purpose. Rapid tests are very useful for quickly iterating on emitter designs, and long-duration tests are useful to properly verify performance before emitters are deployed in the field [119, 120, 109, 110].

Importantly, each type of test relies on different types of suspensions. Rapid tests normally use large particles such as sands because of their large size and relative quickness

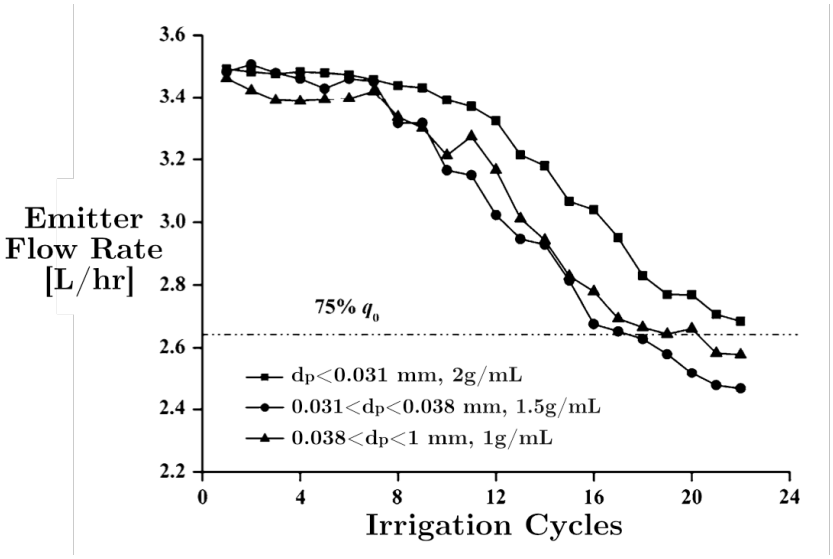

Figure 4.3: Decay of emitter discharge rate over time with 3 different water-based suspension compositions in a common drip emitter geometry across 22 irrigation cycles. Each cycle consisted of 30 minutes of flow and 6 hours of intermission. Particle diameters, d_p, and concentrations of each suspension type listed in the legend. Driving pressure of 0.1MPa. Reproduced from Niu *et al.*[119]

of deposition behavior [119, 120, 121]. Conversely, long-duration tests typically use silt and clay particles to more realistically experiment on the types of particles that are likely to pass through a filter in a drip irrigation system [109, 110]. In the following sections, we will discuss more on the specifics of each type of test.

Importantly, there is the issue of timing; various studies have looked at different cycles, ranging from a continuous test [104], to tests with irrigation and intermission cycles on the same time scale [110, 109], to tests with a short irrigation cycle and long intermission cycle [119]. Notably, the duration of irrigation and intermissions has a profound effect on where particles tend to collect inside the drip emitter. Continuous tests tend to have the lowest particle volume fractions in vortices regions [104], whereas tests with significant intermissions tend to have the highest particle volume fractions in vortices regions [110, 109]. Therefore, it is critical to select a test procedure that matches

the actual operating conditions of planned system deployment, since without such careful considerations, any results may be misleading.

4.3.2 Physical Clogging of Large Particles (Sand, Silt)

In real irrigation systems, the water being used is typically some kind of suspension that may containing sand particles ($> 50\,\mu$m), silt particles ($1-50\,\mu$m) and clay particles ($\leq 1\mu m$) [110, 15]. Importantly, in different locations, the water will contain different types of particles. Larger particles (sand and silt) tend to create a clogging effect due to a direct obstruction of the emitter channel [120, 119]. The process starts with a few particles becoming trapped in a low velocity and low tuerbulent kinetic energy region, and over time, more particles accumulate around them, creating a bridging effect [4]. At small timescales (hours/days), this phenomena will cause a gradual decrease in emitter flow rate, as shown in Figure 4.3 [120, 119]. However, at large timescales (weeks/months), the accumulation of particles of varying sizes fills in all gaps in the granular media and eventually causes a complete clog, like those depicted in Figure 4.4.

Studies of the clogging behavior of large particles in drip emitters is commonly done in literature by conducting rapid clogging tests which consist of multiple stages, using sands suspended in water [118, 119, 121]. In such tests, there is initially a low concentration of sand particles in the test solution, then at each stage, more particles are added to the suspension, increasing the concentration. During each stage, the suspension is flowed through an emitter for a certain duration, and an intermission period occurs before the process repeats [119, 120]. The sand particle sizes can vary for such tests depending on the study, however, the test procedure ISO 8486-1-1997 outlines a standardized procedure designed specifically for drip emitters. Reported by Wei *et al.* [120], this standard ISO testing method consists of adding 250 mg/L of sand to water flowing through an emitter

in 8 different 50-minute stages, with the sand being added at each stage corresponding to a different "grit" rating, based on mean particle size. The first test stage uses "F220" particles, corresponding to sands with a mean diameter of 50 μm; the size is increased in the following stages, with the 8th and final stage introducing 250mg/L of "F60" particles, with a mean diameter of 250 μm [120]. Clogging during such a rapid test is typically evaluated based on variations in the discharge rate, rather than waiting for a total clogging event. Emitters which maintain a flow rate near their typical pure water levels are considered to perform well, and those which drop significantly are considered to perform poorly [118, 119, 121].

Composition of solid phase	**Concentration [mg/L]**	**Particle sizes**	**Other Additions to suspension**	**Source**
Bentonite	200	< 1 μm	NaCl	Bounoua *et al.* [109]
Illite + Calcite	200	< 1 μm	NaCl	Bounoua *et al.* [109]
Kaolinite	500	Mean diameter: 2.65 μm	NaCl **or** $CaCl_2 \cdot 2H_2O$ **or** $Al_2(SO_4)_3 \cdot 16H_2O$	Oliveira *et al.* [110]
Montmorillonite	500	Mean diameter: 2.30 μm	NaCl **or** $CaCl_2 \cdot 2H_2O$ **or** $Al_2(SO_4)_3 \cdot 16H_2O$	Oliveira *et al.* [110]
Sand + Silt + Clay	250-2000 (in stages)	Sand: 50-100 μm Silt: 5-50 μm Clay: <5 μm	None	Niu *et al.* [119]
Sand	250-2000 (in stages)	50-250 μm	None	Wei *et al.* [120]
Sand	500	53-105 μm	None	Fernandes *et al.* [121]
Sand	500	250-500 μm	None	Fernandes *et al.* [121]

Table 4.1: Some examples of the composition of water-based suspensions used in literature for lab-based drip emitter physical clogging studies

4.3.3 Physical Clogging of Small Particles (Clays)

Small particles such as clays and silts pose a different problem. Although the associated clogging effect takes longer to develop, aggregation effects over time can become very significant, and their collection in the emitters is much harder to prevent [119, 122, 123].

A key challenge is that in contrast with larger particles, placing filters with a small enough mesh to catch clay particles (under $\leq 1\mu m$) throughout the system is not an option, due to the huge pressure drops it would cause. Smaller particles also present a different clogging mechanism; instead of becoming rapidly jammed between the teeth, silt and clay particles form deposits over time on the sides of the teeth, mainly in regions of vortices and zones of stagnation [110, 109], as is shown with kaolinite particles in Figure 4.5(a) and (c). This build up of small particles creates additional pressure drop over time, and can eventually lead to the channel becoming entirely clogged [109]. The deposition of small particls is currently a huge limiting factors in widespread drip irrigation implementation, as almost all irrigation water contains such particles, and there is no simple solution to stop them entering emitters. To overcome this challenge, emitters must thus be carefully designed to allow such small particles to flow through and exit with limited deposition.

When it comes to experimental studies, rapid clogging tests are not suitable for studying the deposition of small particles in drip emitters and the potential clogging. This is because these blockages tend to develop over much longer time scales of weeks or months due to their mechanism of gradual particle aggregation on the channel walls, rather than occurring suddenly via a bridging or sieving mechanism like with larger particles [119, 122, 123]. As a result, various different testing approaches have been used to study small particle clogging, all of which consist of flowing a suspension through an emitter across timescales on the order of days or weeks, using emitter flow rate measurement to determine anti-clogging performance [109, 110]. However, unlike with large particles, there is no common (standardized) testing procedure for measuring emitter performance against the deposition and clogging of small particles. A challenge to experiments is that in water used in agriculture, there is a huge variety of different particle types that can be present on the order of 1 micron or less. As a result, throughout literature, studies

with small particles such as clays have been conducted with many different suspension compositions, some of which are listed in Table 1.

It should be noted here that the clogging behavior of small particles is also highly dependent on the ionic strength of the suspension, as ionic strength influences the aggregation behavior of colloidal particles[123, 122, 109, 110]. Some additions used in literature to vary ionic strength are NaCl, $CaCl_2 \cdot 2H_2O$, and $Al_2(SO_4)_3 \cdot 16H_2O$, and the concentration of each present in a suspension may cause variation in results [110]. Ultimately, the wastewater used in irrigation will have different compositions in different parts of the world. As such, confirming the widespread physical anti-clogging performance of a certain emitter design with respect to many different conditions, using various particle types, sizes, and ionic strength is important.

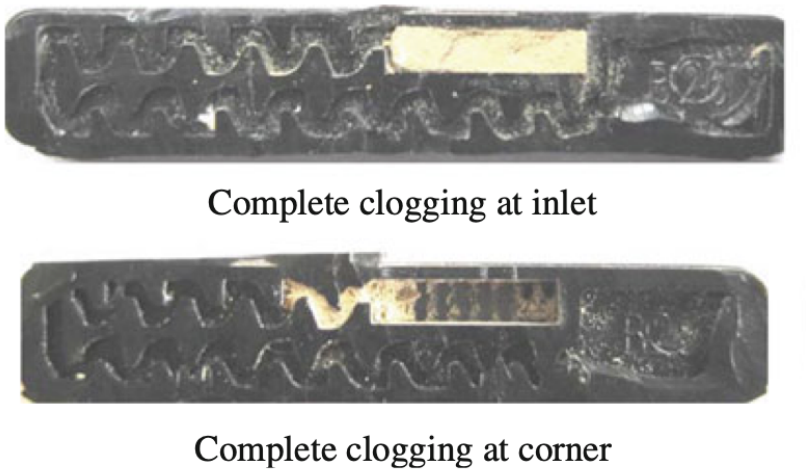

Figure 4.4: Images of two drip emitters with complete physical clogs resulting from a mix of sand, silt, and clay. Top photo shows the development of a clog which originated at the inlet grid, and the bottom photo shows the development of a clog which originated within the labyrinth of a drip emitter. Reproduced from Niu *et al.* [119]

4.4 Strategies to Mitigate Clogging

Currently, there are some strategies which are used to mitigate each of the clogging mechanisms. However, the adoption rate of drip irrigation systems remains very low worldwide (3% of all irrigation in 2020) [91]. This indicates that the problems have not been solved to an adequate extent to make drip irrigation feasible and practical for most situations. Although the clogging rates are heavily dependent on water composition, replacing drip emitters which have become clogged creates a new added cost which can eclipse the system's reduced water spending if clogs occur too often [91, 99]. Regardless, some of the current strategies have been shown to consistently reduce clogging rates, making them an attractive basis for any new designs or strategic additions.

Typically, to prevent physical clogging of large particles such as sands, filters are used upstream of the labyrinth channel, [14] catching the particles in the main tubing and preventing their further transport inside of emitters. This upstream filtration has been shown to improve performance when sands or similar size particles are present [104]. When attempting to prevent deposition of smaller particles, one common strategy is to design emitters which promote turbulent flows internally [14]. This is a promising concept, however, even in the current state-of-the-art systems which utilize turbulent flow, the turbulent kinetic energy in certain regions falls short of the necessary quantity to fully prevent particle deposition and aggregation [110].

Although out of the scope of this review, we should mention that when addressing chemical and biological clogging, a common approach is to add some kind of chemical agent to the mixture that prevents biological growth and/or electromagnetic and chemical effects [14]. For biological clogging prevention, it is typical to use antimicrobial agents or to carry out acidification/chlorification to slow the growth of organic matter within the emitter [14]. To prevent chemical clogging, typically salt or a similar substance is added

to the water, modifying the ionic strength as desired [110].

These strategies, while useful, still leave something desired in terms of overall performance, and this is shown in the lack of widespread adoption of drip irrigation. Small particles like silts and clays still make their way through the current filters, and through agglomeration effects, clog systems at unsustainable rates [14, 110, 109]. As such, improving the understanding the issue of small particle clogging is a promising topic of study, as it is imperative for worldwide water conservation that improvements are made in the area of emitter clogging.

4.4.1 Active Strategies to Prevent Physical Clogging

One of the most straightforward, yet effective active strategies to delay or prevent physical clogging is the flushing of lateral pipes which feed the drip emitters. Typically, drip irrigation systems contain large main lines with smaller lateral branches which redirect water directly to the base of crops, where it flows through a drip emitter [14, 98]. Each lateral branch is capped at its end, and it has been shown that by regularly removing this cap for a period of time and allowing irrigation water to freely flow out of the lateral branch into the surrounding environment without passing through drip emitters, anti-clogging performance is improved in the long run by removing particles which linger in laterals that may later clog drip emitters[124, 125]. One study by Yu *et al.* found that a higher flushing pressure helped to dislodge larger, coarser particles, but a longer flushing time had the greatest effect on removing finer particles [125]. Additionally, laterals which were flushed once a month had on average a 35% longer lifespan than those that were not flushed [125].

One interesting new approach which has been shown to reduce the rate of physical clogging is the use of pulsatile flows. By varying the driving pressure harmonically, it

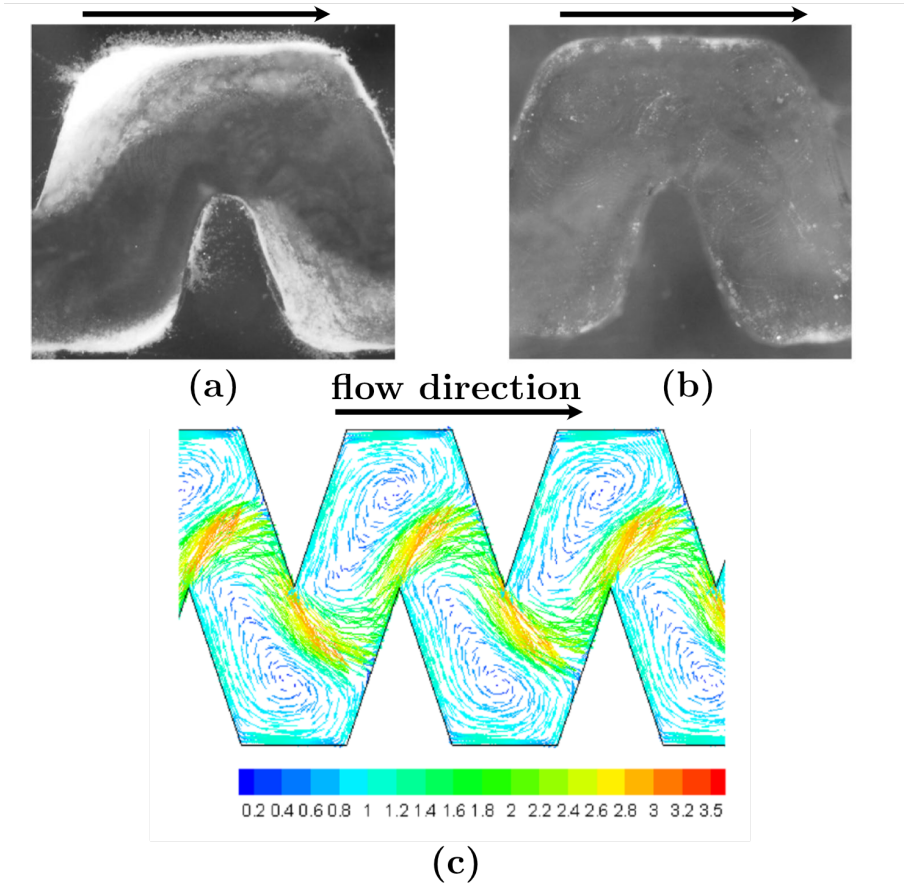

Figure 4.5: Deposition of (a) kaolinite and (b) montmorillonite particles combined with NaCl ions inside a drip emitter after 53 h of testing. Flow direction from left to right. Reproduced from Oliveira *et al.* [110] (c) Velocity field in a drip emitter channel obtained through direct numerical simulation with pure water and a standard k-ϵ model. The color bar is the amplitude of the velocity field in m/s. Flow direction from left to right. Reproduced from Feng *et al.* [104]

has been shown that the increased turbulence in the emitter channel makes deposition of sediments far less frequent, typically occurring only near existing impurities, rather than deposits forming consistently along the back-sides of teeth as in constant pressure systems [126, 121]. As a result, one notable study by Zhang *et al.* showed that over the course of 32 hours, cycling a water-based suspension containing sand particles smaller than 125 μm through a drip emitter resulted in three times less channels clogged when

a pulsatile driving pressure was used, compared to using a constant driving pressure [126]. Although there is a lack of studies on how pulsatile flows could affect clogging for smaller particles (on the order of 1 μm, one could infer that the same principle of reduced particle deposition as a result of increased turbulence would still apply for smaller particles, making pulsatile flows a promising method for future drip emitter technology.

4.4.2 Passive Strategies to Prevent Physical Clogging

Although effective in improving anti-clogging performance, active strategies such as pulsatile flows and lateral flushing require additional regular system maintenance, and in some cases, a higher initial cost [126, 121, 124, 125]. These issues can be prohibitive to system adoption, especially with larger-scale agricultural irrigation operations. Passive, scalable approaches to clogging mitigation would, therefore, significantly simplify the use of drip-irrigation systems. Additionally, there is the possibility that passive strategies could be deployed simultaneously with active strategies to achieve even greater anti-clogging results.

A primary method of passive clog mitigation in drip irrigation is the optimization of drip emitter internal geometry. Strategic changes in channel parameters can be used to induce beneficial flow patterns, such as increasing turbulent kinetic energy in key locations of typical high particle deposition [118, 127]. In systems with long intermissions between irrigation cycles, sediments will settle in the channel during pauses in operation, forming bonds and agglomerates, and if the flow is not properly designed to disrupt sediment formation in certain areas, particles will begin to collect, as shown in Figure 4.5(a) [98, 120, 109]. To address this, the geometry of the drip emitter channel can be optimized to create greater turbulence and flow velocity in vulnerable areas. However, we should emphasize that there are some possible drawbacks that must be considered. One

potential pitfall of geometry optimization is that drip emitters are designed carefully to create a certain pressure drop, which in turn, determines the flow rate. Yet, by changing geometrical parameters, one generally hopes to induce increased turbulence, however, this can result in an undesirably large increase in pressure drop if not done carefully [104]. This could lead to flow slowing down to levels that will not support plant growth, or even shutting off completely. However, if proper considerations are taken, it is possible to design new emitter geometries that optimize flow to reduce clogging while simultaneously maintaining irrigation performance.

Zhang *et al.* used computational fluid dynamics (CFD) to optimize a conventional drip emitter geometry and found that tooth gap width, W (Figure 4.2(b)), seems the most important parameter for decreasing the clogging rate of drip emitters [117]. By minimizing W, the number of vortices in the channel were reduced, and energy was dissipated more uniformly throughout the channel compared to designs with a larger tooth gap, benefiting the emitter's performance against small particle clogging [117]. Other studies have also looked at some new possible designs. Feng *et al.* used CFD analysis to show that a design with a large round arc in the gap between teeth, rather than a flat surface, caused increased turbulent intensity in the region where sand was most likely to collect. Their design resulted in a decreased sand volume fraction in those areas, while still maintaining an acceptable pressure drop [104]. Haosu *et al.* also used CFD to look at novel designs, and came to a similar conclusion that adding a large arc in the tooth-tip facing zone and a small arc at the end of teeth (R in Figure 2b) had the best performance in terms of hydraulics and anti-clogging [127]. These studies, while an interesting basis for any new drip emitter design, mostly rely only on computational methods, and as such, all results should certainly be verified with a variety of different particle types experimentally.

4.5 Conclusion and Future Directions

Clogging is currently a major issue for a wider deployment of drip irrigation. As a result, further advancements in preventing the deposition and agglomeration behavior of silt and clay type particles within drip emitters are strongly needed. These small particles are especially problematic, due to their ability to bypass filtration systems at inlet grids and deposit gradually within emitter channels. Over time, with intermittent flow, these particles can accumulate in low-velocity or stagnant zones, slowly constricting the channel and even completely blocking flow. This gradual process is exacerbated by operational cycles, where intermissions allow sediments to settle and bond. Current prevention strategies have shown promise in mitigating large particle clogging to a significant degree, but still fall short with such small particles. However, some improvements in silt and clay anti-clogging performance can be achieved through optimizing the geometry of the emitter to create turbulence, along with employing active strategies such as lateral flushing and the use of pulsatile flows. Yet while these improvements collectively enhance system performance, they require further refinement to meet the needs of diverse irrigation conditions and expand the feasibility of drip irrigation systems across different scales.

Future advancements may rely on a combination of passive and active methods to optimize clog prevention. In particular, geometry optimization can lead to strong anti-clogging performance, and there are certainly more improvements possible, such as fine-tuning internal geometric features to disrupt sediment deposition even more effectively, reducing vortex zones entirely and greatly enhancing turbulent kinetic energy distribution within the emitter channel. Additionally, for proper validation of new drip emitter designs, comprehensive experimental studies under varying particle types, ionic strengths, and irrigation water compositions are essential. The conventional method of lateral

flushing remains useful for removing small particles from irrigation systems by combining higher flushing pressures with longer durations of flushing, but require action from an operator. When used in combination, flushing and geometry optimization can complement each other: flushing actively clears particles from laterals that may block emitter entrances, while optimized emitter designs reduce the frequency and severity of sediment accumulation inside of drip emitters. By advancing the anti-clogging performance of drip irrigation systems through such integrated approaches, the long-term reliability and adoption of drip irrigation systems can be significantly improved, contributing to global water conservation and sustainable agricultural practices.

Chapter 5

Conclusion

The research presented in this thesis further developed our understanding of suspension flow dynamics under varying geometrical and physical constraints, addressing both fundamental mechanisms and practical applications. We have successfully considered length-based filtering of anisotropic particles suspended in liquids, the clogging of fiber suspensions, and the development of drip irrigation clogging.

In chapter 2, it is shown that by using flat or cylindrical substrates in a dip-coating process, fiber suspensions can be sorted by length or diameter, however, diameter sorting can prove more reliable due to physical constraints preventing fibers larger than a threshold from passing through the filter. Optimal efficiency of length sorting can be achieved using a cylindrical substrate, and with careful consideration of dimensionless parameters such as capillary number, Ca, volume fraction, ϕ and the particle length to substrate diameter ratio $L^* = L/2R_s$. Length sorting between two fiber population is most effective when one population satisfies $L^* \leq 1$ and the other one satisfies $L^* \geq 1$, each of which can be tuned by changing the radius R_s of the cylindrical substrate. Further, volume fraction of the suspension and diameter standard deviation must be minimized to avoid undesired fibers being entrained. Values of Ca for best efficiency depend on the

particular fibers being used. This novel capillary sorting strategy offers highly efficient selective sorting for elongated particles when best practices are used.

In chapter 3, millifluidic devices with controlled geometries were developed to study the clogging behavior of neutrally buoyant, non-Brownian rigid fibers. Experimental and numerical analyses revealed that clogging probability, P_{clog}, depends on fiber length relative to channel width and follows three regimes: (i) for short fibers, $P_{\text{clog}} = 0$ due to reorientation within streamlines; (ii) for long fibers, $P_{\text{clog}} = 1$ as they contact three points in the channel; and (iii) in the transition regime, P_{clog} monotonically increases with fiber length and wall friction. Geometry parameters such as channel width W and radii of curvature $\mathcal{R}_{\text{in}}$ and $\mathcal{R}_{\text{out}}$ shift these regime boundaries as shown in various figures. Specifically, reduction of W and $\mathcal{R}_{\text{out}}$ lead to increased clogging behavior at equivalent fiber lengths. This study establishes a framework for modeling clogging of fiber suspensions around a bend with more complex scenarios, such as flexible fibers or concentrated suspensions.

Finally, chapter 4 reports challenges and advancements in anti-clogging strategies for drip irrigation systems. Typically, during system intermissions, sediments deposit and bond to the internal channel walls, and when flow resumes, there are regions where the flow intensity is not sufficient to wash away agglomerates, eventually forming clogs. However, innovations in emitter design have been shown to reduce physical clogging rates by optimizing geometry to promote self-cleaning flows, reducing vortex zones and increasing turbulent kinetic energy distribution. Studies suggest that such desired flows can be promoted by both minimizing the tooth gap width, and adding arcs to tooth tips and tooth gaps, however, there is no limit to the possible variations of emitter design which may further improve performance. By optimizing emitter geometry to enhance turbulence and disrupt sediment deposition, combined with active strategies like lateral flushing and pulsatile flows, future systems can better manage fine silt and clay particles

that bypass filtration. Comprehensive experimental validation under realistic water compositions and sediment types will be critical to refining these solutions. Integrating and further advancing such methods offers a promising path toward enhancing the reliability, efficiency, and adoption of drip irrigation, contributing to sustainable water management and agricultural productivity.

Bibliography

[1] M. Haw, *Jamming, two-fluid behavior, and "self-filtration" in concentrated particulate suspensions*, *Physical review letters* **92** (2004), no. 18 185506.

[2] H. G. Merkus and H. G. Merkus, *Sieves and sieving*, *Particle size measurements: Fundamentals, practice, quality* (2009) 219–240.

[3] J. C. Crittenden, R. R. Trussell, D. W. Hand, K. J. Howe, and G. Tchobanoglous, *Water treatment: principles and design*. John Wiley & Sons, 2012.

[4] E. Dressaire and A. Sauret, *Clogging of microfluidic systems*, *Soft matter* **13** (2017), no. 1 37–48.

[5] L. J. Gimbert, P. M. Haygarth, R. Beckett, and P. J. Worsfold, *Comparison of centrifugation and filtration techniques for the size fractionation of colloidal material in soil suspensions using sedimentation field-flow fractionation*, *Environmental science & technology* **39** (2005), no. 6 1731–1735.

[6] J. Henry, *Cross flow filtration*, in *Recent developments in separation science*, pp. 205–225. CRC Press, 2018.

[7] D.-H. Jeong, L. Xing, M. K. H. Lee, N. Vani, and A. Sauret, *Deposition and alignment of fiber suspensions by dip coating*, *Journal of Colloid and Interface Science* **650** (2023) 407–415.

[8] B. Dincau, E. Dressaire, and A. Sauret, *Clogging: The self-sabotage of suspensions*, *Physics Today* **76** (2023), no. 2 24–30.

[9] N. Vani, S. Escudier, and A. Sauret, *Influence of the solid fraction on the clogging by bridging of suspensions in constricted channels*, *Soft matter* **18** (2022), no. 36 6987–6997.

[10] A. Sauret, E. C. Barney, A. Perro, E. Villermaux, H. A. Stone, and E. Dressaire, *Clogging by sieving in microchannels: Application to the detection of contaminants in colloidal suspensions*, *Applied Physics Letters* **105** (2014), no. 7.

[11] G. H. Goldsztein and J. C. Santamarina, *Suspension extraction through an opening before clogging*, *Applied physics letters* **85** (2004), no. 19 4535–4537.

[12] A. Marin, H. Lhuissier, M. Rossi, and C. J. Kähler, *Clogging in constricted suspension flows*, *Physical Review E* **97** (2018), no. 2 021102.

[13] C. P. Moore, J. Husson, A. Boudaoud, G. Amselem, and C. N. Baroud, *Clogging of a rectangular slit by a spherical soft particle*, *Physical Review Letters* **130** (2023), no. 6 064001.

[14] M. R. Goyal, *Sustainable Micro Irrigation: Principles and Practices*. CRC Press, 2014.

[15] D. J. Pitts, D. Z. Haman, and A. Smajstria, *Causes and prevention of emitter plugging in micro irrigation systems.*, *Bulletin-Florida Cooperative Extension Service* (1990).

[16] D. Goldberg, B. Gornat, D. Rimon, *et. al.*, *Drip irrigation: principles, design and agricultural practices.*, *Drip irrigation: principles, design and agricultural practices.* (1976).

[17] S. Endoh, J. Koga, and K. Yamaguchi, *The sieving rate of cylinder particles [translated]*, *KONA Powder and Particle Journal* **2** (1984) 7–15.

[18] W. Walton, *Feret's statistical diameter as a measure of particle size*, *Nature* **162** (1948), no. 4113 329–330.

[19] C. Duchêne, V. Filipe, S. Huille, and A. Lindner, *Clogging of microfluidic constrictions by monoclonal antibody aggregates: Role of aggregate shape and deformability*, *Soft matter* **16** (2020), no. 4 921–928.

[20] A. Gans, E. Dressaire, B. Colnet, G. Saingier, M. Z. Bazant, and A. Sauret, *Dip-coating of suspensions*, *Soft Matter* **15** (2019), no. 2 252–261.

[21] S. Palma and H. Lhuissier, *Dip-coating with a particulate suspension*, *Journal of Fluid Mechanics* **869** (2019).

[22] S. N. Shovon, A. Alam, W. Gramlich, and B. Khoda, *Micro-particle entrainment from density mismatched liquid carrier system*, *Scientific Reports* **12** (2022), no. 1 9806.

[23] C. Copeland, C. T. Gabbard, and J. B. Bostwick, *Dip coating of viscous granular suspensions*, *Colloids and Surfaces A: Physicochemical and Engineering Aspects* **674** (2023) 131885.

[24] A. Sauret, A. Gans, B. Colnet, G. Saingier, M. Z. Bazant, and E. Dressaire, *Capillary filtering of particles during dip coating*, *Physical Review Fluids* **4** (2019) 054303.

[25] B. M. Dincau, M. Z. Bazant, E. Dressaire, and A. Sauret, *Capillary sorting of particles by dip coating*, *Physical Review Applied* **12** (2019), no. 1 011001.

[26] B. M. Dincau, E. Mai, Q. Magdelaine, J. Lee, M. Bazant, and A. Sauret, *Entrainment of particles during the withdrawal of a fibre from a dilute suspension*, *Journal of fluid mechanics* **903** (2020) A38.

[27] I. Khalil and B. Khoda, *Sorting of poly-disperse particle by entrapment using liquid carrier system*, *Journal of Manufacturing Science and Engineering* **144** (2022), no. 5 054502.

[28] R. J. Furbank and J. F. Morris, *An experimental study of particle effects on drop formation*, *Physics of Fluids* **16** (2004), no. 5 1777–1790.

[29] C. Bonnoit, T. Bertrand, E. Clément, and A. Lindner, *Accelerated drop detachment in granular suspensions*, *Physics of Fluids* **24** (2012), no. 4.

[30] J. Château, É. Guazzelli, and H. Lhuissier, *Pinch-off of a viscous suspension thread*, *Journal of Fluid Mechanics* **852** (2018) 178–198.

[31] V. Thiévenaz, S. Rajesh, and A. Sauret, *Droplet detachment and pinch-off of bidisperse particulate suspensions*, *Soft matter* **17** (2021), no. 25 6202–6211.

[32] V. Thiévenaz and A. Sauret, *The onset of heterogeneity in the pinch-off of suspension drops*, *Proceedings of the National Academy of Sciences* **119** (2022), no. 13 e2120893119.

[33] P. S. Raux, A. Troger, P. Jop, and A. Sauret, *Spreading and fragmentation of particle-laden liquid sheets*, *Physical Review Fluids* **5** (2020), no. 4 044004.

[34] D.-H. Jeong, L. Xing, J.-B. Boutin, and A. Sauret, *Particulate suspension coating of capillary tubes*, *Soft Matter* **18** (2022), no. 42 8124–8133.

[35] R. Krechetnikov and G. Homsy, *Experimental study of substrate roughness and surfactant effects on the landau-levich law*, *Physics of Fluids* **17** (2005), no. 10.

[36] E. Rio and F. Boulogne, *Withdrawing a solid from a bath: How much liquid is coated?*, *Adv. Colloid Interface Sci.* **247** (2017) 100–114.

[37] L. Landau and B. Levich, *Dragging of a liquid by a moving plate*, *Acta Physicochimica URSS* **17** (1942) 42–54.

[38] B. Derjaguin, *On the thickness of the liquid film adhering to the walls of a vessel after emptying*, *Progress in Surface Science* **43** (1993), no. 1 134–137.

[39] D. A. White and J. A. Tallmadge, *Static menisci on the outside of cylinders*, *J. Fluid Mech.* **23** (1965), no. 2 325–335.

[40] D. A. White and J. A. Tallmadge, *A theory of withdrawal of cylinders from liquid baths*, *AIChE Journal* **12** (1966), no. 2 333–339.

[41] D. Quéré, *FLUID COATING ON a FIBER*, *Annual Review of Fluid Mechanics* **31** (jan, 1999) 347–384.

[42] C. E. Colosqui, J. F. Morris, and H. A. Stone, *Hydrodynamically driven colloidal assembly in dip coating*, *Physical review letters* **110** (2013), no. 18 188302.

[43] H. C. Mayer and R. Krechetnikov, *Landau-levich flow visualization: Revealing the flow topology responsible for the film thickening phenomena*, *Physics of Fluids* **24** (may, 2012) 052103.

[44] D.-H. Jeong, A. Kvasnickova, J.-B. Boutin, D. Cébron, and A. Sauret, *Deposition of a particle-laden film on the inner wall of a tube*, *Physical Review Fluids* **5** (2020), no. 11 114004.

[45] J. E. Butler and B. Snook, *Microstructural dynamics and rheology of suspensions of rigid fibers*, *Annual Review of Fluid Mechanics* **50** (2018) 299–318.

[46] S. N. Bounoua, P. Kuzhir, and E. Lemaire, *Shear reversal experiments on concentrated rigid fiber suspensions*, *Journal of Rheology* **63** (2019), no. 5 785–798.

[47] D.-H. Jeong, M. K. H. Lee, V. Thiévenaz, M. Z. Bazant, and A. Sauret, *Dip coating of bidisperse particulate suspensions*, *Journal of Fluid Mechanics* **936** (2022) A36.

[48] C. Duty, C. Ajinjeru, V. Kishore, B. Compton, N. Hmeidat, X. Chen, P. Liu, A. A. Hassen, J. Lindahl, and V. Kunc, *What makes a material printable? a viscoelastic model for extrusion-based 3d printing of polymers*, *Journal of Manufacturing Processes* **35** (2018) 526–537.

[49] T. Beran, T. Mulholland, F. Henning, N. Rudolph, and T. A. Osswald, *Nozzle clogging factors during fused filament fabrication of spherical particle filled polymers*, *Additive Manufacturing* **23** (2018) 206–214.

[50] S. He, N. Joseph, S. Feng, M. Jellicoe, and C. L. Raston, *Application of microfluidic technology in food processing*, *Food & function* **11** (2020), no. 7 5726–5737.

[51] A. Sauret, K. Somszor, E. Villermaux, and E. Dressaire, *Growth of clogs in parallel microchannels*, *Physical Review Fluids* **3** (2018), no. 10 104301.

[52] H. M. Wyss, D. L. Blair, J. F. Morris, H. A. Stone, and D. A. Weitz, *Mechanism for clogging of microchannels*, *Phys. Rev E* **74** (2006), no. 6 061402.

[53] B. Dersoir, M. R. de Saint Vincent, M. Abkarian, and H. Tabuteau, *Clogging of a single pore by colloidal particles*, *Microfluidics and Nanofluidics* **19** (2015) 953–961.

[54] C. M. Cejas, F. Monti, M. Truchet, J.-P. Burnouf, and P. Tabeling, *Particle deposition kinetics of colloidal suspensions in microchannels at high ionic strength*, *Langmuir* **33** (2017), no. 26 6471–6480.

[55] Q. Liu, B. Zhao, and J. C. Santamarina, *Particle migration and clogging in porous media: a convergent flow microfluidics study*, *Journal of Geophysical Research: Solid Earth* **124** (2019), no. 9 9495–9504.

[56] N. Delouche, A. Schofield, and H. Tabuteau, *Dynamics of progressive pore clogging by colloidal aggregates*, *Soft Matter* **16** (2020), no. 43 9899–9907.

[57] B. Dincau, C. Tang, E. Dressaire, and A. Sauret, *Clog mitigation in a microfluidic array via pulsatile flows*, *Soft Matter* **18** (2022), no. 9 1767–1778.

[58] A. Hafez, Q. Liu, T. Finkbeiner, R. A. Alouhali, T. E. Moellendick, and J. C. Santamarina, *The effect of particle shape on discharge and clogging*, *Scientific Reports* **11** (2021), no. 1 1–11.

[59] N. Vani, S. Escudier, and A. Sauret, *Influence of the solid fraction on the clogging by bridging of suspensions in constricted channels*, *Soft matter* **18** (2022), no. 36 6987–6997.

[60] N. Vani, S. Escudier, D.-H. Jeong, and A. Sauret, *Role of the constriction angle on the clogging by bridging of suspensions of particles*, *Physical Review Research* **6** (2024), no. 3 L032060.

[61] A. Marin and M. Souzy, *Clogging of noncohesive suspension flows*, *Annual Review of Fluid Mechanics* **57** (2024).

[62] L. Chen, K. X. Wang, and P. S. Doyle, *Effect of internal architecture on microgel deformation in microfluidic constrictions*, *Soft Matter* **13** (2017), no. 9 1920–1928.

[63] J. Mancuso and W. Ristenpart, *Stretching of red blood cells at high strain rates*, *Physical Review Fluids* **2** (2017), no. 10 101101.

[64] B. G. Compton and J. A. Lewis, *3d-printing of lightweight cellular composites*, *Advanced materials* **26** (2014), no. 34 5930–5935.

[65] J. R. Raney, B. G. Compton, J. Mueller, T. J. Ober, K. Shea, and J. A. Lewis, *Rotational 3d printing of damage-tolerant composites with programmable mechanics*, *Proceedings of the National Academy of Sciences* **115** (2018), no. 6 1198–1203.

[66] X. Tian, A. Todoroki, T. Liu, L. Wu, Z. Hou, M. Ueda, Y. Hirano, R. Matsuzaki, K. Mizukami, K. Iizuka, *et. al.*, *3d printing of continuous fiber reinforced polymer composites: development, application, and prospective*, *Chinese Journal of Mechanical Engineering: Additive Manufacturing Frontiers* **1** (2022), no. 1 100016.

[67] B. P. Croom, A. Abbott, J. W. Kemp, L. Rueschhoff, L. Smieska, A. Woll, S. Stoupin, and H. Koerner, *Mechanics of nozzle clogging during direct ink writing of fiber-reinforced composites*, *Additive Manufacturing* **37** (2021) 101701.

[68] M. Saadi, A. Maguire, N. T. Pottackal, M. S. H. Thakur, M. M. Ikram, A. J. Hart, P. M. Ajayan, and M. M. Rahman, *Direct ink writing: a 3d printing technology for diverse materials*, *Advanced Materials* **34** (2022), no. 28 2108855.

[69] M. E. Villalba, M. Daneshi, and D. M. Martinez, *Characterizing jamming of dilute and semi-dilute fiber suspensions in a sudden contraction and a t-junction*, *Physics of Fluids* **35** (2023), no. 12.

[70] B. Bräsel, M. Geiger, J. Linkhorst, and M. Wessling, *Transport and clogging dynamics of flexible rods in pore constrictions*, *Soft Matter* **20** (2024), no. 34 6767–6778.

[71] R. B. Manners, M. Doyle, and M. Small, *Structure and hydraulics of natural woody debris jams*, *Water Resources Research* **43** (2007), no. 6 W06432.

[72] I. Schalko, L. Schmocker, V. Weitbrecht, and R. M. Boes, *Laboratory study on wood accumulation probability at bridge piers*, *Journal of Hydraulic Research* **58** (2020), no. 4 566–581.

[73] G. K. Batchelor, *Slender-body theory for particles of arbitrary cross-section in Stokes flow*, *Journal of Fluid Mechanics* **44** (Nov., 1970) 419–440.

[74] O. G. Harlen, R. R. Sundararajakumar, and D. L. Koch, *Numerical simulations of a sphere settling through a suspension of neutrally buoyant fibres*, *Journal of Fluid Mechanics* **388** (June, 1999) 355–388.

[75] H. Manikantan and D. Saintillan, *Subdiffusive transport of fluctuating elastic filaments in cellular flows*, *Physics of Fluids* **25** (2013), no. 7 073603.

[76] W. Russel, E. Hinch, L. G. Leal, and G. Tieffenbruck, *Rods falling near a vertical wall*, *Journal of Fluid Mechanics* **83** (1977), no. 2 273–287.

[77] B. Semin, J.-P. Hulin, and H. Auradou, *Influence of flow confinement on the drag force on a static cylinder*, *Physics of Fluids* **21** (2009), no. 10 103604.

[78] L. Li, H. Manikantan, D. Saintillan, and S. E. Spagnolie, *The sedimentation of flexible filaments*, *Journal of Fluid Mechanics* **735** (nov, 2013) 705–736, [arXiv:1306.4692].

[79] R. L. Schiek and E. S. Shaqfeh, *Cross-streamline migration of slender brownian fibres in plane poiseuille flow*, *Journal of Fluid Mechanics* **332** (1997) 23–39.

[80] A. Farutin, T. Piasecki, A. M. Słowicka, C. Misbah, E. Wajnryb, and M. L. Ekiel-Jeżewska, *Dynamics of flexible fibers and vesicles in poiseuille flow at low reynolds number*, *Soft Matter* **12** (2016), no. 35 7307–7323.

[81] T. Nguyen and H. Manikantan, *Cross-streamline migration and near-wall depletion of elastic fibers in micro-channel flows*, *Soft Matter* **20** (2024), no. 8 1725–1735.

[82] H. Berthet, M. Fermigier, and A. Lindner, *Single fiber transport in a confined channel: Microfluidic experiments and numerical study*, *Physics of Fluids* **25** (2013), no. 10 103601.

[83] M. Nagel, P.-T. Brun, H. Berthet, A. Lindner, F. Gallaire, and C. Duprat, *Oscillations of confined fibres transported in microchannels*, *Journal of Fluid Mechanics* **835** (2018) 444–470.

[84] J. S. Wexler, P. H. Trinh, H. Berthet, N. Quennouz, O. Du Roure, H. E. Huppert, A. Lindner, and H. A. Stone, *Bending of elastic fibres in viscous flows: the influence of confinement*, *Journal of fluid mechanics* **720** (2013) 517–544.

[85] B. Chakrabarti, C. Gaillard, and D. Saintillan, *Trapping, gliding, vaulting: transport of semiflexible polymers in periodic post arrays*, *Soft Matter* **16** (2020), no. 23 5534–5544.

[86] H. Manikantan and D. Saintillan, *Buckling transition of a semiflexible filament in extensional flow*, *Physical Review E* **92** (oct, 2015) 041002.

[87] E. A. Schnorr Filho, N. C. Lima, and E. M. Franklin, *Resolved cfd-dem simulations of the hydraulic conveying of coarse grains through a very-narrow elbow*, *Powder Technology* **395** (2022) 811–821.

[88] R. L. Schiek and E. S. G. Shaqfeh, *A nonlocal theory for stress in bound, Brownian suspensions of slender, rigid fibres*, *Journal of Fluid Mechanics* **296** (Aug., 1995) 271–324.

[89] R. L. Schiek and E. S. G. Shaqfeh, *Cross-streamline migration of slender Brownian fibres in plane Poiseuille flow*, *Journal of Fluid Mechanics* **332** (Feb., 1997) 23–39.

[90] A. A. Evans, S. E. Spagnolie, D. Bartolo, and E. Lauga, *Elastocapillary self-folding: Buckling, wrinkling, and collapse of floating filaments*, *Soft Matter* **9** (2013), no. 5 1711–1720.

[91] U.-W. UNESCO, *2020: United nations world water development report*, tech. rep., 2020.

[92] A. Boretti and L. Rosa, *Reassessing the projections of the world water development report*, *NPJ Clean Water* **2** (2019), no. 1 1–6.

[93] A. Dinar, A. Tieu, and H. Huynh, *Water scarcity impacts on global food production*, *Global Food Security* **23** (2019) 212–226.

[94] T. Sauer, P. Havlík, U. A. Schneider, E. Schmid, G. Kindermann, and M. Obersteiner, *Agriculture and resource availability in a changing world: The role of irrigation*, *Water Resources Research* **46** (2010), no. 6.

[95] I. Mazher, S. Fayyaz-ul Hassan, H. Tamoor, N. Aadal, M. Azeem, T. Muhammad, *et. al.*, *Evaluation of comparative water use efficiency of furrow and drip irrigation systems for off-season vegetables under plastic tunnel.*, *International Journal of Agriculture and Crop Sciences (IJACS)* **7** (2014), no. 4 185–190.

[96] P. Shamshery, R.-Q. Wang, D. V. Tran, and A. G. Winter V, *Modeling the future of irrigation: A parametric description of pressure compensating drip irrigation emitter performance*, *PloS one* **12** (2017), no. 4 e0175241.

[97] C. A. Madramootoo and J. Morrison, *Advances and challenges with micro-irrigation*, *Irrigation and Drainage* **62** (2013), no. 3 255–261.

[98] M. R. Goyal, V. K. Chavan, and V. K. Tripathi, *Principles and management of clogging in micro irrigation*, vol. 1. CRC Press, 2016.

[99] J. Enciso and D. Porter, *Basics of microirrigation.* Texas Cooperative Extension, The Texas A & M University System, 2005.

[100] Q. Wei, Y. Shi, W. Dong, G. Lu, and S. Huang, *Study on hydraulic performance of drip emitters by computational fluid dynamics*, *Agricultural Water Management* **84** (2006), no. 1-2 130–136.

[101] Y. Dazhuang, Y. Peiling, R. Shumei, L. Yunkai, and X. Tingwu, *Numerical study on flow property in dentate path of drip emitters*, *New Zealand Journal of Agricultural Research* **50** (2007), no. 5 705–712.

[102] Z. Wei, M. Cao, X. Liu, Y. Tang, and B. Lu, *Flow behaviour analysis and experimental investigation for emitter micro-channels*, *Chinese journal of mechanical engineering* **25** (2012), no. 4 729–737.

[103] D. Karmeli, *Classification and flow regime analysis of drippers*, *Journal of agricultural engineering research* **22** (1977), no. 2 165–173.

[104] J. Feng, Y. Li, W. Wang, and S. Xue, *Effect of optimization forms of flow path on emitter hydraulic and anti-clogging performance in drip irrigation system*, *Irrigation Science* **36** (2018), no. 1 37–47.

[105] J. Narain and A. G. Winter V, *A hybrid computational and analytical model of inline drip emitters*, *Journal of Mechanical Design* **141** (2019), no. 7 1–13.

[106] G. W. Anyango, G. D. Bhowmick, and N. Sahoo Bhattacharya, *A critical review of irrigation water quality index and water quality management practices in micro-irrigation for efficient policy making*, *Desalination and Water Treatment* **318** (2024) 100304.

[107] J. Sokol, J. Narain, J. Costello, T. McLaurin, D. Kumar, and A. Winter, *Analytical model for predicting activation pressure and flow rate of pressure-compensating inline drip emitters and its use in low-pressure emitter design*, *Irrigation Science* **40** (03, 2022) 1–21.

[108] F. Nakayama and D. Bucks, *Water quality in drip/trickle irrigation: a review*, *Irrigation science* **12** (1991), no. 4 187–192.

[109] S. Bounoua, S. Tomas, J. Labille, B. Molle, J. Granier, P. Haldenwang, and S. N. Izzati, *Understanding physical clogging in drip irrigation: in situ, in-lab and numerical approaches*, *Irrigation Science* **34** (2016), no. 4 327–342.

[110] F. de Oliveira, R. Lavanholi, A. de Camargo, J. Frizzone, N. A. Mouheb, S. Tomas, and B. Molle, *Influence of concentration and type of clay particles on dripper clogging*, *Irrigation & Drainage Systems Engineering* **6** (2017), no. 1 5.

[111] B. Zhou, T. Wang, Y. Li, and V. Bralts, *Effects of microbial community variation on bio-clogging in drip irrigation emitters using reclaimed water*, *Agricultural Water Management* **194** (2017) 139–149.

[112] J. Qian, H. Horn, J. Tarchitzky, Y. Chen, S. Katz, and M. Wagner, *Water quality and daily temperature cycle affect biofilm formation in drip irrigation devices revealed by optical coherence tomography*, *Biofouling* **33** (2017), no. 3 211–221.

[113] Y. Dazhuang, B. Zhihui, M. Rowan, G. Likun, R. Shumei, and Y. Peiling, *Biofilm structure and its influence on clogging in drip irrigation emitters distributing reclaimed wastewater*, *Journal of Environmental Sciences* **21** (2009), no. 6 834–841.

[114] D. J. Hills, F. M. Nawar, and P. M. Waller, *Effects of chemical clogging on drip-tape irrigation uniformity*, *Transactions of the ASAE* **32** (1989), no. 4 1202–1206.

[115] P. Shamshery and A. G. Winter, *Shape and form optimization of on-line pressure-compensating drip emitters to achieve lower activation pressure*, *Journal of Mechanical Design* **140** (2018), no. 3 035001.

[116] J. Narain, *A hybrid computational and analytical model of irrigation drip emitters*, master's thesis, Massachusetts Institute of Technology, Cambridge, MA, June, 2017.

[117] W. Zhang, L. Yang, J. Wang, and X. Zhang, *Analysis of flow channel structure parameter and optimization study on tooth spacing of drip irrigation tape*, *Water (Basel)* **14** (2022), no. 11 1694–.

[118] X. Qiu, G. Chen, H. Wang, C. Wang, and J. Wang, *Vertical optimisation of tooth shape to improve the anti-clogging performance of emitters in drip irrigation systems*, *Biosystems Engineering* **233** (2023), no. 1 193–203.

[119] W. Niu, L. Liu, and X. Chen, *Influence of fine particle size and concentration on the clogging of labyrinth emitters*, *Irrigation Science* **31** (07, 2013).

[120] Q. Wei, Y. Shi, G. Lu, W. Dong, and S. Huang, *Rapid evaluations of anticlogging performance of drip emitters by laboratorial short-cycle tests*, *Journal of Irrigation and Drainage Engineering* **134** (2008), no. 3 298–304.

[121] C. N. Fernandes and J. C. C. Saad, *Evaluation of pulsating pressure and emitter position in preventing drip emitters from clogging*, *Journal of irrigation and drainage engineering* **148** (2022), no. 3.

[122] F. C. de Oliveira, R. Lavanholi, A. P. de Camargo, N. Ait-Mouheb, J. A. Frizzone, S. Tomas, and B. Molle, *Clogging of drippers caused by suspensions of kaolinite and montmorillonite clays*, *Irrigation Science* **38** (2020), no. 1 65–75.

[123] R. Lavanholi, F. C. Oliveira, A. P. d. Camargo, J. A. Frizzone, B. Molle, N. Ait-Mouheb, and S. Tomas, *Methodology to evaluate dripper sensitivity to clogging due to solid particles: an assessment*, *The Scientific World Journal* **2018** (2018).

[124] J. Puig-Bargués, G. Arbat, M. Elbana, M. Duran-Ros, J. Barragán, F. R. de Cartagena, and F. Lamm, *Effect of flushing frequency on emitter clogging in microirrigation with effluents*, *Agricultural Water Management* **97** (2010), no. 6 883–891.

[125] L. Yu, N. Li, X. Liu, Q. Yang, and J. Long, *Influence of flushing pressure, flushing frequency and flushing time on the service life of a labyrinth-channel emitter*, *Biosystems Engineering* **172** (2018) 154–164.

[126] L. Zhang, P. Wu, D. Zhu, and C. Zheng, *Effect of pulsating pressure on labyrinth emitter clogging*, *Irrigation Science* **35** (07, 2017).

[127] S. Haosu, L. Yunkai, F. Ji, H. Liu, and Y. Liu, *Effects of flow path boundary optimizations on particle transport in drip irrigation emitters*, *Irrigation and Drainage* **65** (2016), no. 4 417–425, https://onlinelibrary.wiley.com/doi/pdf/10.1002/ird.2017.